

# Stochastic-deterministic modeling of bed load transport in shallow water flow over erodible slope: Linear stability analysis and numerical simulation



Patricio Bohorquez<sup>a,\*</sup>, Christophe Ancey<sup>b</sup>

<sup>a</sup> Área de Mecánica de Fluidos, Departamento de Ingeniería Mecánica y Minera, CEA Tierra, Universidad de Jaén, Campus de las Lagunillas, 23071, Jaén, Spain

<sup>b</sup> Environmental Hydraulics Laboratory, École Polytechnique Fédérale de Lausanne, 1015 Lausanne, Switzerland

## ARTICLE INFO

### Article history:

Received 2 February 2015

Revised 26 April 2015

Accepted 18 May 2015

Available online 22 May 2015

### Keywords:

Saint-Venant-Exner

Stochastic bed load transport

ClawPack/SharpClaw

Hydrodynamic stability

Anti-dunes

## ABSTRACT

In this article we propose a stochastic bed load transport formulation within the framework of the frictional shallow-water equations in which the sediment transport rate results from the difference between the entrainment and deposition of particles. First we show that the Saint-Venant-Exner equations are linearly unstable in most cases for a uniform base flow down an inclined erodible bed for Shields numbers in excess of the threshold for incipient sediment motion allowing us to compute noise-induced pattern formation for Froude numbers below 2. The wavelength of the bed forms are selected naturally due to the absolute character of the bed instability and the existence of a maximum growth rate at a finite wavelength when the particle diffusivity coefficient and the water eddy viscosity are present as for Turing-like instability. A numerical method is subsequently developed to analyze the performance of the model and theoretical results through three examples: the simulation of the fluctuations of the particle concentration using a stochastic Langevin equation, the deterministic simulation of anti-dunes formation over an erodible slope in full sediment-mobility conditions, and the computation of noise-induced pattern formation in hybrid stochastic-deterministic flows down a periodic flume. The full non-linear numerical simulations are in excellent agreement with the theoretical solutions. We conclude highlighting that the proposed depth-averaged formulation explains the developments of upstream migrating anti-dunes in straight flumes since the seminar experiments by Gilbert (1914).

© 2015 Elsevier Ltd. All rights reserved.

## 1. Introduction

Since the earliest developments on bed load transport equations, the most common approach taken in computational river dynamics for routing sediment has involved the Exner equation and bed load transport equations, i.e. algebraic expressions relating the mean sediment flux  $\bar{q}_s$  to the water conditions (e.g., the dimensionless Shields number  $Sh$ ). In classical theories of sediment transport, the water flow is mostly described as a nearly uniform flow under equilibrium conditions [46,75,80]. The resulting governing equations are the one- or two-dimensional Saint-Venant equations or, more recently, the three-dimensional Navier–Stokes equations [78]. In his recent paper reviewing the last decade of research on river bed stability, Colombini [27] noted that one of the current challenges is to substitute the classic Exner equation with a probabilistic

version. Stochastic partial differential equations are an emerging field not yet standard in sedimentation engineering but are becoming increasingly utilized [69,73]. In this article, we supplement the one-dimensional Saint-Venant equations with the stochastic form of the Exner equation recently proposed by Ancey and Heyman [5], we study for the first time the linear stability properties of the system and we verify the theoretical results by means of full non-linear numerical simulations of noise-induced pattern formation using a finite volume method for hybrid stochastic-deterministic flows.

A common practice in sedimentation engineering is to distinguish between flows with intense and moderate sediment transport rates [e.g. 54]. The *partial mobility regime* is encountered when  $Sh < 2 Sh_{cr}$  [42], with  $Sh_{cr}$  the critical Shields number for the onset of sediment motion. It corresponds to situations in which part of the bed sediment is mobilized by the water stream and so, the resulting sediment transport rate is low to moderate. The *full mobility regime* describes situations in which all the bed surface takes an active part in the sediment transport process, often under full bank conditions. Classical bed load transport equations such as the Meyer-Peter & Mueller, Ashida & Michiue and Fernandez Luque & van Beek formulas have

\* Corresponding author. Tel.: +34 953 211 872; fax: +34 953 212 870.

E-mail addresses: [patricio.bohorquez@ujaen.es](mailto:patricio.bohorquez@ujaen.es) (P. Bohorquez), [christophe.ancey@epfl.ch](mailto:christophe.ancey@epfl.ch) (C. Ancey).

been applied to both regimes. Applying these deterministic equations to the partial mobility regime leads to excessive errors and uncertainties in the prediction of the transported sediment volume, especially on long time scales (e.g., weeks or more) [68]. Applied to the full mobility regime, these equations usually provide the correct trend, but even in this favorable case, they cannot predict the bed load flux with an error lower than 200% [37]. We think that the improvement of bed load transport models calls for a more refined framework rather than a refinement of algebraic sediment transport equations (e.g., by increasing the number of variables of the problem). A clear impediment to greater accuracy has so far been the occurrence of wide fluctuations of the sediment transport rate and the development of bed forms. Both processes are intertwined and it is difficult to evaluate one without studying the other. In this paper, we use the stochastic framework for bed load transport proposed by Ancey et al. [4]. Within this framework, the sediment transport rate is defined as the difference between the entrainment and deposition rates and so, it can vary locally significantly over time depending on the flow conditions, bed slope, and transport of particles in the close neighborhood. This framework is well suited to the partial mobility regime as it does not directly relate the water discharge and particle flux, but defines the latter as a random variable. We will show that it is also consistent with the existing bed load transport equations for the full mobile regime: indeed, we have observed that the average sediment transport rate exhibits the same exponential dependence on the Shields number as classical formulas and other erosion-deposition models for  $Sh \gg Sh_{cr}$ .

Even in the simplest case of the one-dimensional Saint-Venant equations, substantial numerical difficulties arise when coupling the classical Exner equation with algebraic bed load discharge equations. For instance, two of the three system eigenvalues vanish [60], which requires a careful treatment of critical conditions and the absence of sediment motion. Schemes used for strongly coupled or decoupled numerical schemes are also the object of intense debates [29,45,66,72]. Interestingly here, we will see that the erosion-deposition formulation for bed load transport allows us to readily extend previous finite volume methods for frictional shallow water equations similar to what has been done for computing the suspended load in dilute flows, see Bohorquez and Fernández-Feria [14]. A simple strategy allows us to readily incorporate the stochastic equations for bed load transport into the numerical codes previously developed for frictional shallow-water flows on fixed beds [13,14].

The paper is organized as follows: the problem under investigation is summarized in Section 2. The linear stability properties of the mean balance equations are explored in Section 3. Next, Section 4 is devoted to the description of the hybrid finite-differences/finite-volume method and the numerical simulations. Accuracy and performance are evaluated by comparing numerical simulations with available theoretical solutions [3,4,43]. We also study the evolution of infinitesimal disturbances on a uniform base flow down an inclined plane, which leads to pattern formation and anti-dunes. Following Bohorquez [13], new analytical solutions are built and compared with numerical simulations. Conclusions are finally presented in Section 5.

## 2. Physical problem under investigation

### 2.1. Saint-Venant Exner equations: entrainment-deposition model

For one-space variable problems, the simplest morphodynamic model comprises the shallow-water (Saint-Venant) equations for the conservation of mass and momentum of the water phase and the Exner equation for the continuity equation of the bed [37]:

$$\frac{\partial h}{\partial t} + \frac{\partial h\bar{v}}{\partial x} = 0, \tag{1}$$

$$\frac{\partial h\bar{v}}{\partial t} + \frac{\partial h\bar{v}^2}{\partial x} + gh\frac{\partial h}{\partial x} = -gh\frac{\partial y_b}{\partial x} - \frac{\tau_b}{\rho} + \frac{\partial}{\partial x}\left(vh\frac{\partial \bar{v}}{\partial x}\right), \tag{2}$$

$$(1 - \zeta_b)\frac{\partial y_b}{\partial t} = D - E \cong -\frac{\partial \bar{q}_s}{\partial x}, \tag{3}$$

in which  $h(x, t) = y_s - y_b$  denotes the flow depth,  $y_b(x, t)$  and  $y_s(x, t)$  are the positions of the bed and free surfaces,  $\bar{v}$  is the depth-averaged velocity,  $x$  is the downstream position,  $t$  is time,  $\rho$  is the water density,  $\tau_b$  is the bottom shear stress,  $\zeta_b$  is the bed porosity,  $\bar{q}_s$  is the average bed load transport rate (see (7) below), and  $D$  and  $E$  represent the deposition and entrainment rates, respectively. The bed slope is defined as  $\tan \theta = -\partial_x y_b$ . In most models based on (1)–(3), the governing equations are closed by empirical relationships for the flow resistance  $\tau_b$  and sediment transport rate  $\bar{q}_s$ , both being functions of the flow variables  $\bar{v}$  and  $h$ , and additional parameters (e.g., bed roughness and slope). Physically, this means that the sediment phase is the slave of the water phase and this dependence is justified by the momentum transfers from the water to the sediment phases [8,9]. The extra term  $\partial_x(vh\partial_x\bar{v})$  in the momentum balance equation (2) represents a simple depth-averaged Reynolds stress [64].

### 2.2. Stochastic approach

Here we take a different approach to sediment transport. Following Einstein [33], we consider that sediment transport results from the imbalance between erosion and entrainment. Originally, Einstein [33] developed a Lagrangian viewpoint and expressed the erosion and deposition rates from statistical features of particle trajectories. More recently, Ancey et al. [4] used the framework of jump Markov processes for describing the random time variation in the number of moving particles  $n$  in a given volume of control. This Eulerian approach led them to express the entrainment and deposition rates as a function of the mean *particle activity*  $\langle \gamma \rangle$  (i.e., the volume of moving particles  $n$  per unit bed area):  $E = \lambda + \mu \langle \gamma \rangle$  and  $D = \sigma \langle \gamma \rangle$ . The angular brackets  $\langle \gamma \rangle$  refer to the ensemble average of the random variable  $\gamma$ . The parameters  $\lambda$ ,  $\mu$  and  $\sigma$  were called the particle entrainment, the collective entrainment, and the deposition coefficients. Note the asymmetry in the expressions of the entrainment and deposition rates, which result from the differences in the physical processes involved.

As  $n$  and  $\gamma$  are random variables, they are characterized by their probability distribution function  $P_n(x, t)$  and  $P_\gamma(x, t)$ . Ancey et al. [4] used the theory of birth-death Markov processes for deriving the governing equation of the number of moving particles  $n$ , more exactly its probability distribution. To make the problem more tractable, Ancey and Heyman [5] worked not with the distribution  $P_n(x, t)$ , but with the Poisson representation

$$P_n(x, t) = \int_{\mathbb{R}_+} P_a(x, t) \frac{e^{-a} a^n}{n!} da,$$

where  $a$  is called the Poisson rate and  $P_a$  is its probability distribution function. The Poisson representation can be thought of as a Laplace transform for probabilities distributions, which makes it possible to work with continuous random variables (here  $a$ ) instead of discrete random variable (here  $n$ ). Indeed, like in continuum mechanics, it is easier to work with local continuous variables than with global and discrete variables. Ancey and Heyman [5] introduced the particle activity as the limit of the volume occupied by the particles when the length  $\Delta x$  of the control volume tends to 0

$$\gamma = \lim_{\Delta x \rightarrow 0} \frac{nV_p}{B\Delta x},$$

where  $V_p = \pi d^3/6$  is the typical particle volume,  $B$  is the width of the control volume,  $d$  is the mean particle diameter. Similarly, they took

the continuum limit of  $a$  and introduced the Poisson density  $b$

$$b = \lim_{\Delta x \rightarrow 0} \frac{a}{\Delta x}.$$

An interesting property of the Poisson representation is that the  $a$ - and  $n$  moments are linked, and so are the moments of  $b$  and  $\gamma$ . In particular, we have

$$\langle \gamma \rangle = \frac{\langle b \rangle V_p}{B}. \quad (4)$$

Within the framework of continuous Markov processes, Ancey and Heyman [5] found that the governing equation for  $b$  is a stochastic advection diffusion equation with a source term and colored noise

$$\frac{\partial b}{\partial t} + \frac{\partial}{\partial x}(\bar{u}_s b) - \frac{\partial^2}{\partial x^2}(D_u b) = \lambda' - \kappa b + \sqrt{2\mu b} \xi_b \quad (5)$$

where  $\xi_b$  is a Gaussian noise term such that  $\langle \xi_b(x, t) \xi_b(x', t') \rangle = \hat{\delta}(x - x') \hat{\delta}(t - t')$  (with  $\hat{\delta}$  Kronecker's symbol),  $\bar{u}_s$  is the mean particle velocity, and  $D_u$  is the particle diffusivity, which is linked to the particles' velocity fluctuations. Solving Eq. (5) for  $b$  allows us to fully characterize the fluctuations of the particle activity, hence the instantaneous sediment transport rate  $q_s = \gamma \bar{u}_s$ .

We can also deduce the mean sediment transport rate and make insightful links between the stochastic erosion-deposition formulation (5) and the Exner equation (3). Taking the ensemble average of (5) and using the Itô convention, we end up with the governing equation for  $\langle \gamma \rangle$

$$\frac{\partial}{\partial t} \langle \gamma \rangle + \frac{\partial}{\partial x}(\bar{u}_s \langle \gamma \rangle) - \frac{\partial^2}{\partial x^2}(D_u \langle \gamma \rangle) = \lambda - \kappa \langle \gamma \rangle, \quad (6)$$

where  $\lambda = \lambda' V_p / B$  (or  $\lambda' = \lambda B / V_p$ ). A caveat is in order: the treatment of the colored noise term  $\sqrt{2\mu b} \xi_b$  in (5) can be achieved following two different approaches [38]: in the Itô interpretation, the value of  $b$  is taken before the jump; an important consequence is that  $\langle \sqrt{2\mu b} \xi_b \rangle = 0$ . Another possibility is the Stratonovich interpretation, which takes the mean of  $b$  before and after the jump (and in that case  $\langle \sqrt{2\mu b} \xi_b \rangle > 0$ ). The latter interpretation is often seen as the most natural choice physically [69], but unfortunately it leads to substantial mathematical difficulties when trying to solve stochastic differential equations analytically. So, following the usage in the physics of reaction-diffusion problems [38], we have adopted the Itô convention. Following Furbish et al. [36], we can define the bulk sediment transport rate as  $\bar{q}_s = \bar{u}_s \langle \gamma \rangle - \partial_x(D_u \langle \gamma \rangle)$ . It is then straightforward to show that (6) is equivalent to

$$\frac{\partial \bar{q}_s}{\partial x} = E(x, t) - D(x, t) - \frac{\partial}{\partial t} \langle \gamma \rangle. \quad (7)$$

Note also that when setting  $D_u = 0$  in (6), we recover the equation for the particle number  $n = \langle \gamma \rangle / V_p$  [22,33,49]. Substituting (7) into (3) and neglecting the time variation in the particle concentration  $\partial_t \langle \gamma \rangle$ , we arrive at the standard version of Exner equation,  $(1 - \zeta_b) \partial_t y_b = -\partial_x \bar{q}_s$ , which is valid provided that the ratio  $\bar{q}_s / h \bar{v}$  remains small [30]. Thus to leading order, the bed evolution  $\partial_t y_b$  is controlled by the gradient  $\partial_x \bar{q}_s$ .

In the following, we will solve the Saint-Venant-Exner equations (1)–(3). In the Exner equation, the entrainment and deposition rates are expressed as functions of the mean particle activity:  $E = \lambda + \mu \langle \gamma \rangle$  and  $D = \sigma \langle \gamma \rangle$ , respectively. The mean particle activity  $\langle \gamma \rangle$  can be derived from the deterministic advection diffusion equation (6). When we are also interested in determining the strength of the sediment transport rate fluctuations, we solve the stochastic partial differential equation (5), which provides the Poisson density  $b$ . There is no back Poisson transformation and so it is not possible to infer the probability distribution  $P_\gamma$  directly from the Poisson density  $b$ , but there are alternative ways of characterizing  $P_\gamma$ . For instance, we can relate the  $\gamma$  and  $b$  averages using (4) [5]. Higher-order moments are more difficult to express explicitly [3]. The last step prior

to numerical solutions concerns the closure equations, which specify the dependence of the parameters  $\tau_b$ ,  $\nu$ ,  $\bar{u}_s$ ,  $\lambda$  and  $\sigma$  involved in the Saint-Venant-Exner equations.

### 2.3. Closure equations

The hydraulic resistance  $\tau_b$  in the momentum balance equation (2) is evaluated using the Darcy–Weisbach friction factor  $f$  as

$$\frac{\tau_b}{\rho} = \frac{f}{8} \bar{v} |\bar{v}|. \quad (8)$$

Setting the bed roughness to  $4d$  ( $d$  is the mean grain diameter) and assuming a channel width much larger than the flow depth with hydraulic diameter  $D_h = 4h$  [46], we calculate  $f$  as a function of the relative roughness in fully developed turbulent flow and rough regime as [25]

$$\frac{1}{\sqrt{f}} = -2 \log_{10} \left( \frac{\delta^2}{3.71} \right), \quad \delta^2 = \frac{d}{h}. \quad (9)$$

The particle velocity  $\bar{u}_s$  is computed using an expression dimensionally consistent with Bagnold [9] law,  $\bar{u}_s \propto \sqrt{\tau_b}$ . Direct numerical simulations using the discrete element method [32] and flume experiments [56] have shown that the following nondimensional relation accurately fits the particle velocity data

$$\frac{\bar{u}_s}{\sqrt{gd(s-1)}} = m_0 + m_1 \left( \sqrt{\frac{Sh}{Sh_{cr}}} - 1 \right), \quad (10)$$

where  $Sh$  is the Shields number,

$$Sh = \frac{|\tau_b|}{\rho(s-1)gd}, \quad (11)$$

$Sh_{cr}$  denotes the critical Shields number for incipient motion and  $s = \rho_p / \rho$  represents the sediment-to-liquid density ratio (typically  $s = 2.65$  for gravel in water). Substituting the Shields definition (11) into (10), using (8) and multiplying by the factor  $\sqrt{d(s-1)}/h$ , we end up with

$$\frac{\bar{u}_s}{\sqrt{gh}} = (m_0 - m_1) \sqrt{s-1} \delta + \sqrt{\frac{f m_1^2}{8 Sh_{cr}}} Fr, \quad (12)$$

in which  $Fr = \bar{v} / \sqrt{gh}$  denotes the Froude number. Taking into account that  $m_0 \approx 0.88$  and  $m_1 \approx 1.44$  for  $s \approx 2$  [32], we get  $(m_0 - m_1) \sqrt{s-1} \delta \approx 0.77 \delta$ . When  $\delta \ll 1$ , it yields

$$\frac{\bar{u}_s}{\sqrt{gh}} \approx \beta Fr \quad \text{with} \quad \beta \equiv \min \left( \sqrt{\frac{f m_1^2}{8 Sh_{cr}}}, 1 \right). \quad (13)$$

This empirical relationship is consistent with Chatanantavet et al. [23] who obtained  $0.6 \leq \beta \leq 0.8$  for bedrock channels. We have used the physical constraint  $\beta \leq 1$  in (13) to prevent the unrealistic situation in which the liquid moves slower than the carried sediment. Assuming a constant value of  $f$ , we used the simplified equation  $\bar{u}_s = \beta \bar{v}$ . The dependence of  $\beta$  on  $Sh_{cr}$  and  $f(\delta)$  explains the disparity of values encountered in the literature.

For steady uniform flows, the erosion rate  $E$  balances the deposition flux  $D$  in (7). The equilibrium or saturated value of the particle concentration satisfies the relation

$$\langle \gamma \rangle_{ss} = \frac{\lambda}{\kappa} = \frac{\lambda}{\sigma - \mu}. \quad (14)$$

In turbulent regime, Fernandez Luque and van Beek [34] showed that

$$\frac{\langle \gamma \rangle_{ss} d^2}{V_p} \propto Sh - Sh_{cr}. \quad (15)$$

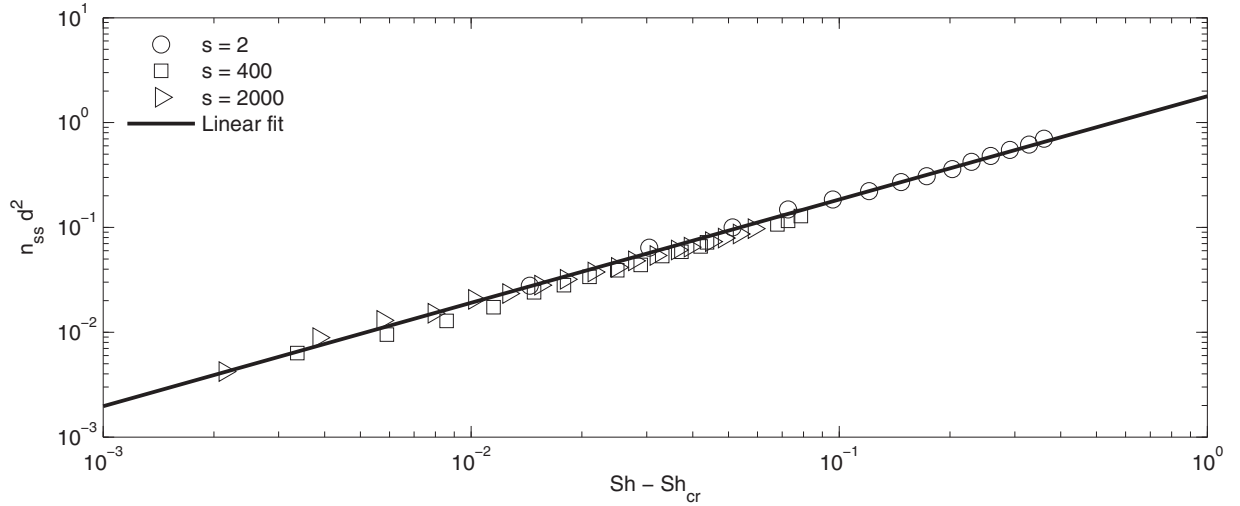


**Fig. 1.** Fit of the numerical results by Durán et al. [32] for the steady-state surface density of moving particles  $n_{ss} = \langle \gamma \rangle_{ss} / V_p$ . The solid line represents the regression equation  $n_{ss} d^2 = 10^{0.2368} (Sh - Sh_{cr}) \approx 1.725 (Sh - Sh_{cr})$  with  $Sh_{cr} = 0.12$ .

This equation is consistent with direct numerical simulations by Durán et al. [32] who obtained a constant of proportionality of 1.725 for  $Sh - Sh_{cr} \leq 0.5$  that lies really close to the value of 1.8 for  $Sh - Sh_{cr} \leq 0.1$  inferred by Fernandez Luque and van Beek [34]. Interestingly this constant is independent of the density ratio  $s$  that ranges from 2 to 2000 in their simulations, see Fig. 1. In the present study, we use closure equations for  $\lambda$  and  $\kappa$  consistent with (15). The key problem is that the available data do not allow us to fit all of the parameters. As a first approximation, we thus assume that the collective entrainment vanishes ( $\mu = 0$ ) and so  $\kappa = \sigma$ . In these conditions, the deposition rate can be formulated in terms of dimensional analysis as

$$\kappa = c_d \sqrt{\frac{(s-1)g}{d}} \quad (16)$$

in which the coefficient  $c_d = 0.094 \pm 0.006$  was inferred from the particle flight time [22,56]. Similarly, the erosion rate is given by

$$\lambda = \frac{c_e^* V_p}{\rho_p d^3} \frac{\tau_b - \tau_{cr}}{\sqrt{(s-1)gd}} = \frac{c_e V_p}{\rho d^3} \frac{\tau_b - \tau_{cr}}{\sqrt{(s-1)gd}}, \quad (17)$$

where  $c_e^* = c_e s$  and  $\tau_{cr}$  is the critical shear stress corresponding to  $Sh_{cr}$ . Substituting (16)–(17) into (14), we arrive at

$$\frac{\langle \gamma \rangle_{ss} d^2}{V_p} = s \frac{c_e^*}{c_d} (Sh - Sh_{cr}) = \frac{c_e}{c_d} (Sh - Sh_{cr}). \quad (18)$$

We set  $c_e = s c_e^* = 1.75 c_d$  according to Fig. 1 and [34].

The eddy viscosity  $\nu$  in (2) is usually neglected in ideal shallow water flows [31]. However, numerical simulations of free surface instabilities in frictional flows down inclined planes have shown that a non-negligible eddy viscosity  $\nu$  is required to avoid the development of unphysical short wavelength instabilities as well as to reproduce the non-linear steady-state shape of roll waves [11,15,18,64]. In this study the main role of the eddy viscosity is to prevent the development of discontinuities in the free surface, which allows us to evaluate the free surface slope in the presence of jumps and steps of the bed elevation. A rough estimation of the eddy viscosity is given by  $\nu \approx \nu_t h \sqrt{\tau_b / \rho}$  with the non-dimensional parameter  $\nu_t$  in the range of  $4 \leq \nu_t \leq 18$  [18].

The particle diffusivity  $D_u$  in (5)–(6) arises from the second moment of the probability density function of particle displacements [36] and has been recently quantified near incipient motion conditions by Heyman et al. [43]. The parametric dependence on the flow variables remains unexplored to our knowledge and, because of this, we treat  $D_u$  as a degree of freedom in our study. We shall show its

relevance on pattern formation in Section 3.4 proposing plausible values.

### 3. Linear stability analysis

We now consider a steady, uniform flow of depth  $H$ , velocity  $V$  and mean particle activity  $\langle \gamma \rangle_{ss} = \lambda / \kappa$  down an erodible bed inclined at a constant angle  $\theta$  with respect to the horizontal. Before describing some numerical results for this apparently simple problem, we present a spatio-temporal stability analysis of the steady uniform base flow [48], which is subsequently employed to verify the outputs of the numerical simulations by comparing the theoretical and numerical growth rates of infinitesimal perturbations. A similar benchmark was proposed in Bohorquez and Rentschler [15] for the flow of kinematic waves down fixed beds, which is associated with the spontaneous formation of natural roll waves [13]. The linear stability properties of the equations at hand have not been explored beforehand. They shed new light on the reliability of the mean equations when studying patterns formation.

#### 3.1. Dimensional groups

Using the characteristic values  $\{V, H, \theta, \langle \gamma \rangle_{ss}\}$  to make variables dimensionless

$$\begin{aligned} u &\leftarrow \frac{\tilde{v}}{V}, & \eta &\leftarrow \frac{h}{H}, & z &\leftarrow \frac{y_b}{H}, & \phi &\leftarrow \frac{\langle \gamma \rangle}{\langle \gamma \rangle_{ss}}, & \hat{x} &\leftarrow \frac{x \tan \theta}{H}, \\ \hat{t} &\leftarrow \frac{t V \tan \theta}{H}, \end{aligned} \quad (19)$$

by taking into account the closure equations presented in Section 2.3 and dropping the hat decoration, we rewrite (1)–(3) and (6) in the dimensionless following form:

$$\begin{aligned} \frac{\partial \eta}{\partial t} + \frac{\partial \eta u}{\partial x} &= 0, \\ Fr^2 \left( \frac{\partial \eta u}{\partial t} + \frac{\partial \eta u^2}{\partial x} \right) + \eta \frac{\partial \eta}{\partial x} - \frac{\partial}{\partial x} \left( \nu \eta \frac{\partial u}{\partial x} \right) &= -\eta \frac{\partial z}{\partial x} - u^2, \\ \frac{\partial z}{\partial t} &= k_e \left( \phi - \frac{u^2 - u_*^2}{1 - u_*^2} \right), \\ \frac{\partial \phi}{\partial t} + \beta \frac{\partial \phi u}{\partial x} - \mathcal{D} \frac{\partial^2 \phi}{\partial x^2} &= k_d \left( \frac{u^2 - u_*^2}{1 - u_*^2} - \phi \right). \end{aligned} \quad (20)$$

Our mean equations resemble the deterministic model by Vesipa et al. [76] that catches correctly the anti-dune regime. Their model

also comprises an erosion–deposition sediment transport equation based on the areal concentration of the moving particles [65] together with Dressler [31] equations for the water phase. It embeds the erosion–deposition equation developed by Charru [21] to study ripple formation. A novelty of our mean sediment transport equation is the inclusion of the particle diffusivity  $\mathcal{D}$  that allows the onset of Turing-like instability [69]. Furthermore, its mathematical structure is analogous to the suspended sediment transport equation proposed by Balmforth and Vakil [11] to predict cyclic steps—the next bed form transition after anti-dunes formation [20]. Taking into account the supporting theoretical results and numerical simulations presented in this article, we believe that one of the main advantages of this family of sediment transport models is the capability to study pattern formation with  $Fr < 2$ , a regime in which classical Saint-Venant-Exner are stable. Furthermore, classical Saint-Venant-Exner equations are recovered under equilibrium conditions with the sediment load given by  $\bar{q}_s = \bar{u}_s(\gamma)_{ss}$  [34].

The dimensionless groups in (19) that govern the flow dynamics are

$$Fr = \frac{V}{\sqrt{gH}}, \quad k_e = \frac{\pi c_e(1-u_*^2)}{6(1-\zeta_b)\delta Fr\sqrt{s-1}}, \quad k_d = \frac{c_d(s-1)}{\delta Fr \tan\theta},$$

$$\mathcal{D} = \frac{D_u \tan\theta}{HV}, \quad u_* = \sqrt{\frac{\tau_{cr}}{\tau_b}}, \quad (21)$$

and  $\nu = \nu Fr^2 \tan\theta / (HV)$ . In subcritical, critical and supercritical flows the Froude number of the base flow is  $Fr < 1$ ,  $Fr = 1$  and  $Fr > 1$ , respectively, and its value is fixed by the Darcy–Weisbach friction factor  $f$  and the bed slope:  $Fr = \sqrt{8 \tan\theta / f}$ . It is found that, for the same slope and Froude number, the grain size plays a key role in the problem as the erosion  $k_e$  and deposition  $k_d$  parameters (21) are much larger in sand rivers (for which we have  $\delta \ll 1$ ) than in gravel bed rivers (for which  $\delta \sim O(10^{-1})$ ). The parameter  $u_*$  varies from 1 to 0 as the shear stress increases from incipient conditions ( $\tau_b \approx \tau_{cr}$ ) to the full mobility regime ( $\tau_b \gg \tau_{cr}$ ). Alternatively, the transport stage parameter  $T = \tau_b / \tau_{cr} - 1$  is zero at inception of sediment motion and raises above zero when  $\tau_b > \tau_{cr}$ . The sediment-to-water density ratio and bed porosity are set to  $s = 2.65$  and  $\zeta_b = 0.36$  two values that are typical of a random close packing of spherical quartz particles in water. The values  $c_d = 0.1$  and  $c_e = 1.75 c_d$  are used in the following (as explained in Section 2.3).

A further reduction of the parameter space is possible by taking into account the following relations between the Shields number  $Sh$ , the bed slope angle  $\theta$ ,  $Fr$  and  $\delta^2$ :

$$Sh = \frac{\tau_b}{\rho(s-1)gd} = \frac{f Fr^2}{8(s-1)\delta^2} = \frac{\tan\theta}{(s-1)\delta^2}, \quad \tan\theta = \frac{f Fr^2}{8}, \quad (22)$$

in which the friction factor  $f$  depends only on  $\delta^2$  for high Reynolds number flows, see Eq. (9). The transport stage parameter  $T$ , or equivalently  $u_*$  (21), can be expressed in terms of  $Sh_{cr}$  as  $u_* = (1+T)^{-1/2} = (Sh_{cr}/Sh)^{1/2} \leq 1$ , where the critical Shields number for the onset of sediment motion  $Sh_{cr}(Re_*)$  is a function of the particle Reynolds number  $Re_* = \delta^2 \sqrt{f/8} Re$  or the flow Reynolds number. Without any loss of generality we set  $Sh_{cr} = 0.03$  from now on.

As a consequence the parameter space of the dimensional groups (21) can be substantially reduced to  $\delta$ ,  $Fr$  and  $\mathcal{D}$ . The rest of the coefficients  $\{s, c_d, c_e, Sh_{cr}\}$  and  $\{u_*, \tan\theta, \beta\}$  are taken constants or functions of them. We keep  $\mathcal{D}$  as a relevant input parameter in the absence of closure equation for the particle diffusivity coefficient. In doing so, we can parametrize the neutral curves of roll waves and erosion–deposition instabilities in the temporal stability analysis as  $Fr_{rw}(\delta, \mathcal{D})$  and  $Fr_{ed}(\delta, \mathcal{D})$ , as shown below and in Fig. 2.

### 3.2. Dispersion relation

Substituting the expansion  $(z, \phi, \eta, u) = (-x, 1, 1, 1) + \epsilon(z', \phi', \eta', u')$  into (20), retaining only the terms of the order  $O(\epsilon)$  and dropping the prime decoration, we end up with the linear perturbation equations:

$$\frac{\partial \eta}{\partial t} + \frac{\partial \eta}{\partial x} + \frac{\partial u}{\partial x} = 0,$$

$$Fr^2 \left( \frac{\partial u}{\partial t} + \frac{\partial u}{\partial x} \right) + \frac{\partial \eta}{\partial x} - \nu \frac{\partial^2 u}{\partial x^2} = -\frac{\partial z}{\partial x} + \eta - 2u,$$

$$\frac{\partial z}{\partial t} = k_e \left( \phi - \frac{2u}{1-u_*^2} \right),$$

$$\frac{\partial \phi}{\partial t} + \beta \left( \frac{\partial u}{\partial x} + \frac{\partial \phi}{\partial x} \right) - \mathcal{D} \frac{\partial^2 \phi}{\partial x^2} = k_d \left( \frac{2u}{1-u_*^2} - \phi \right). \quad (23)$$

Linearizing the non-dimensional eddy viscosity in (23), it reads  $\nu = \nu_t Fr (\tan\theta)^{3/2}$ .

The linear system of partial differential equations (23) admits solutions in the form  $(z, \phi, \eta, u) = \bar{T} \exp[ia(x-ct)]$  where the eigenvector is denoted by  $\bar{T} \equiv (\zeta, \Phi, \Gamma, U)^T$ , the real downstream wavenumber by  $a$  and the complex wave speed by  $c = c_r + ic_i$  [48]. The base flow is unstable (stable) when the growth rate is positive ( $c_i > 0$  (negative  $c_i < 0$ )). The sign of  $c_r$  determines whether the perturbation moves downstream ( $c_r > 0$ ) or upstream ( $c_r < 0$ ) and whether it moves faster than the base flow ( $c_r > 1$ ). This leads to the following eigenvalue problem:

$$\left[ -iac \begin{pmatrix} 1 & 0 & 0 & 0 \\ 0 & 1 & 0 & 0 \\ 0 & 0 & 1 & 0 \\ 0 & 0 & 0 & Fr^2 \end{pmatrix} + ia \begin{pmatrix} 0 & 0 & 0 & 0 \\ 0 & \beta & 0 & \beta \\ 0 & 0 & 1 & 1 \\ 1 & 0 & 1 & Fr^2 \end{pmatrix} - a^2 \begin{pmatrix} 0 & 0 & 0 & 0 \\ 0 & -\mathcal{D} & 0 & 0 \\ 0 & 0 & 0 & 0 \\ 0 & 0 & 0 & -\nu \end{pmatrix} + \begin{pmatrix} 0 & -k_e & 0 & \frac{2k_e}{1-u_*^2} \\ 0 & k_d & 0 & -\frac{2k_d}{1-u_*^2} \\ 0 & 0 & 0 & 0 \\ 0 & 0 & -1 & 2 \end{pmatrix} \right] \cdot \begin{bmatrix} \zeta \\ \Phi \\ \Gamma \\ U \end{bmatrix} = 0. \quad (24)$$

The first row of (24) establishes a relation between the eigenvector components  $\zeta$ ,  $\Phi$  and  $U$ , allowing for the reduction of the eigenproblem (24) by means of

$$\zeta = \frac{ik_e}{ac} \Phi - \frac{i2k_e}{ac(1-u_*^2)} U. \quad (25)$$

Note that the perturbation of the bed elevation  $\zeta$  can be provoked not only by a fluctuation of the particle concentration  $\Phi$  but also by the water velocity  $U$ . Substituting (25) into the last row of (24), we get

$$\left[ -iac \begin{pmatrix} 1 & 0 & 0 \\ 0 & 1 & 0 \\ 0 & 0 & Fr^2 \end{pmatrix} + ia \begin{pmatrix} \beta & 0 & \beta \\ 0 & 1 & 1 \\ \frac{ik_e}{ac} & 1 & Fr^2 - \frac{i2k_e}{ac(1-u_*^2)} \end{pmatrix} - a^2 \begin{pmatrix} -\mathcal{D} & 0 & 0 \\ 0 & 0 & 0 \\ 0 & 0 & -\nu \end{pmatrix} + \begin{pmatrix} k_d & 0 & -\frac{2k_d}{1-u_*^2} \\ 0 & 0 & 0 \\ 0 & -1 & 2 \end{pmatrix} \right] \cdot \begin{bmatrix} \Phi \\ \Gamma \\ U \end{bmatrix} = 0. \quad (26)$$

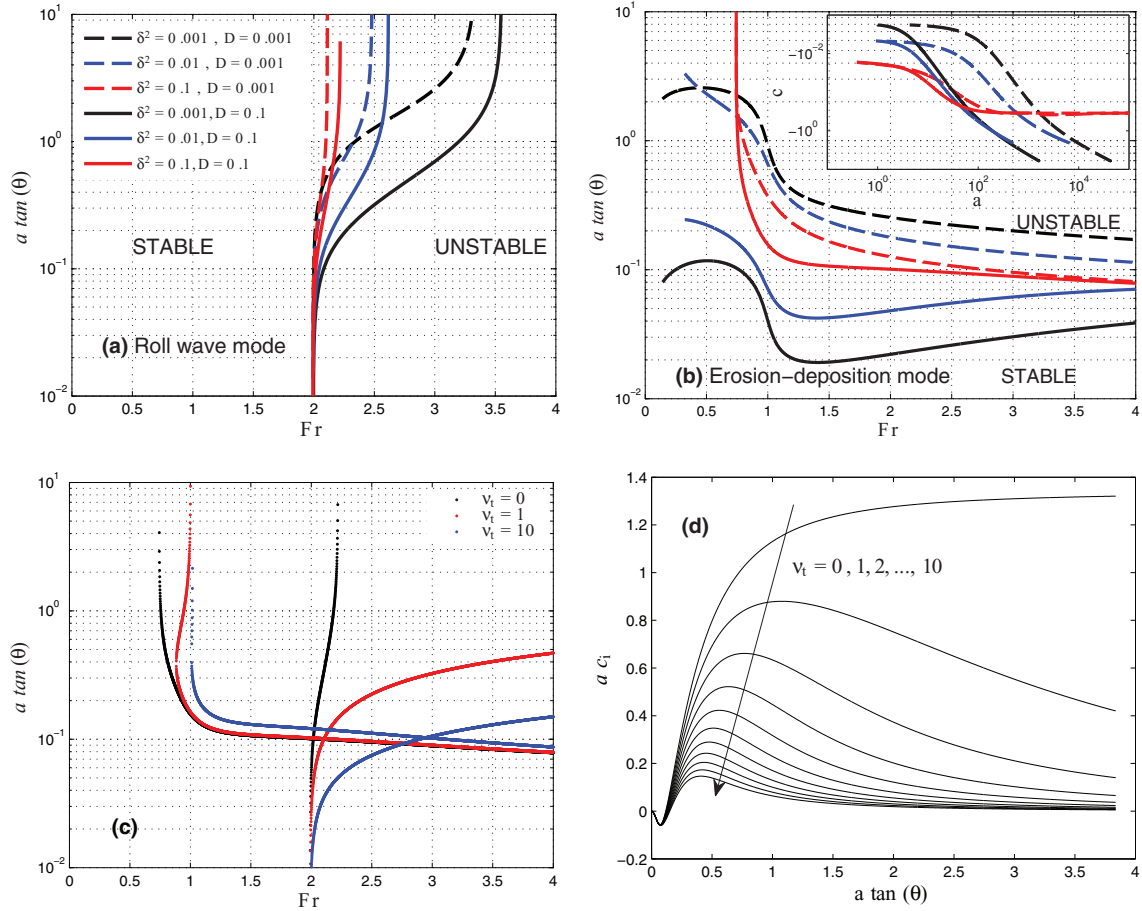


**Fig. 2.** Neutral curve of (a) the roll wave mode and (b) the erosion-deposition instability in the  $(Fr, a)$ -plane as a function of  $\delta$  and  $\mathcal{D}$ . The neutral curve is obtained by setting  $c_i = 0$  in the dispersion relation (27). (c) Sensitivity of the neutral curve for  $\delta^2 = \mathcal{D} = 0.1$  with  $0 \leq \nu_t \leq 10$ . Note that when  $\nu_t > 0$  there is a cutoff wavenumber in the roll wave spectrum. (d) Growth rate of the erosion-deposition mode as a function of the wavenumber for the same range of parameter values as in (c) with  $Fr = 1.2$  showing a maximum when  $\nu_t > 0$  that corresponds with the most unstable wavelength.

The dispersion relation is obtained by setting the determinant of (26) to zero. For instance, in the zero eddy viscosity case, i.e.  $\nu = 0$ , it reads

$$\mathbb{D}(a, c) \equiv c \left[ \frac{i+a}{c-1} - 2i - aFr^2(c-1) \right] - \frac{ik_e}{u_*^2 - 1} \left[ \frac{2k_d + ia(u_*^2 - 1)\beta}{a^2\mathcal{D} + k_d + ia(\beta - c)} - 2 \right] = 0. \quad (27)$$

The dispersion relation (27) can be employed to evaluate the temporal growth rate of spatial disturbance of known wavelength (or wavenumber).

### 3.3. Neutral curves

Also, the dispersion relation (27) serves to obtain the neutral curve, which determines the conditions for the growth of linear instabilities. Using (21)–(22), we fixed the parameters  $\delta^2$  and  $\mathcal{D}$  and solved (27) for the growth rate  $c$  by varying the Froude number  $Fr$  and the wavenumber  $a$ . Fig. 2 shows the existence of two neutral curves associated with the onset of morphodynamic and hydrodynamic instabilities. The hydrodynamic one has a neutral curve starting at  $a = 0$  and  $Fr \approx 2$ . It is the most intuitive mode and leads to the formation of *roll waves* as for non-erodible beds [11,15,64]. As  $a$  grows, the Froude number required for the onset of roll waves is slightly larger. This effect is particularly evident in Fig. 2(a) with the curve related to  $\delta^2 = 10^{-3}$  because the critical Froude number raises approximately from 2 to 3.5 when  $a$  increases. The second mode is associ-

ated with the instability of the bed and will be referred to as *erosion-deposition mode*. It covers the subcritical regime ( $Fr < 1$ ) as shown by Fig. 2(b). Similar to the hydrodynamic instability, it depends at leading order on the grain-size to flow-depth ratio  $\delta^2$ . At large values of  $\delta^2 \sim O(10^{-1})$ , i.e. for gravel bed streams, the critical Froude number pertaining to the onset of erosion-deposition waves is defined by the asymptote occurring at  $Fr_{ed} \approx 0.7 - 0.75$ . The nondimensional particle diffusivity  $\mathcal{D}$  does not affect  $Fr_{ed}$  significantly, but its influence on the bypass wavenumber is marked. Interestingly, a larger particle diffusivity  $\mathcal{D}$  makes the system more unstable by decreasing the bypass frequency, which is a desirable effect as  $D_u$  is related to the second moment of velocity fluctuations [5]. Diffusion may amplify instabilities instead of dampening them under a slight noise-induced perturbation. The erosion-deposition neutral curves are truncated at low  $Fr$  in most cases because of the condition  $u_* \leq 1$  (i.e.  $Sh \geq Sh_{cr}$ ) imposed in our developments. This makes it possible to define the critical Froude number

$$Fr_{ed}^2 = 8(s-1) \frac{\delta^2}{f(\delta)} Sh_{cr}. \quad (28)$$

Interestingly, we found out that the flow down an inclined plane is unconditionally unstable for the proposed model. In most cases, instabilities can develop as soon as the Shields number  $Sh$  is above the threshold of sediment motion  $Sh_{cr}$ .

### 3.4. Absolute instability: particle diffusivity as cause of river anti-dunes

In this section we show that particle diffusion is a necessary physical process in the developments of anti-dunes with critical Froude

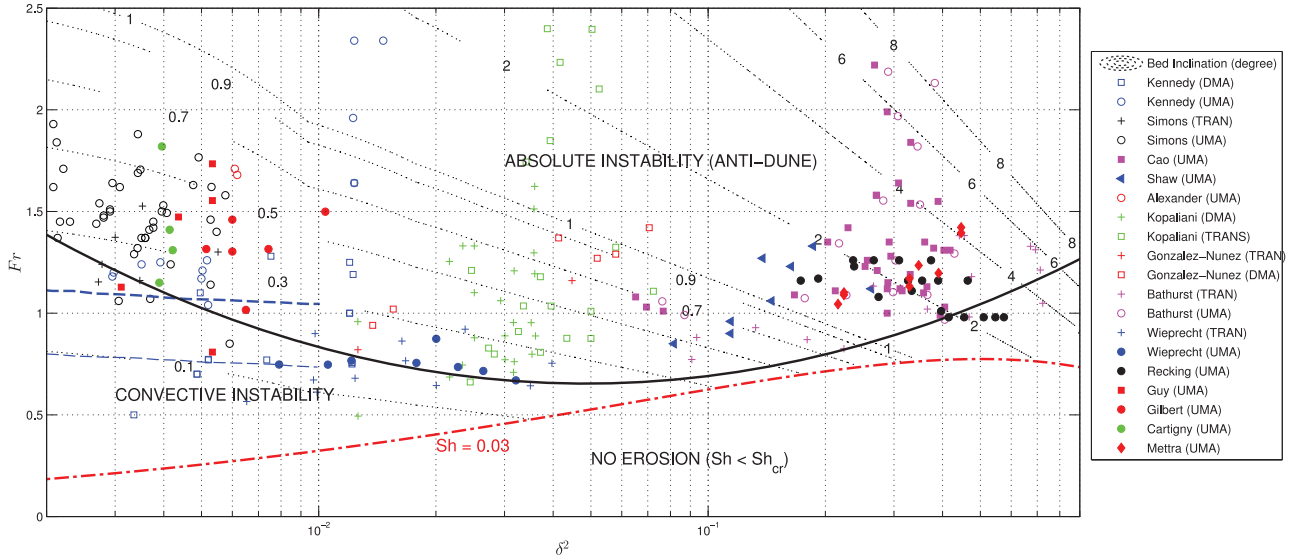


**Fig. 3.** Summary of available experiments on anti-dunes in the plane  $\{\delta^2, Fr\}$ , see [39,51] and references in [19,20,62,67]. UMA and DMA denote two-dimensional upstream and three-dimensional downstream migrating anti-dunes, respectively, and TRAN corresponds with transition bed forms (mostly standing waves). The thick solid line is the approximate bound defining the region of existence of anti-dunes. The red dotted-dashed line represents the curve with constant Shields number  $Sh_{cr} = 0.03$ . The thin and thick dashed lines are the neutral curve for the onset of convective and absolute instability obtained by Vesipa et al. [77]. The dotted curves represent isolines with constant bottom angles as shown in their labels (in degrees). (For interpretation of the references to color in this figure legend, the reader is referred to the web version of this article.)

numbers between 0.5 and 1.8 depending on the relative roughness or grain-size to flow-depth ratio  $\delta^2 = d/H$ , see Fig. 3. A proper selection of the particle diffusivity coefficient  $\mathcal{D}$  in the mean model equations (19) allows us to predict the anti-dune transition (solid line in Fig. 3) in the wide range of relative roughness  $10^{-3} \leq \delta^2 \leq 0.5$  in agreement with numerous experiments, see [19,20,39,51,67] and references therein. The linear stability analysis by Vesipa et al. [76] originally reproduced the anti-dune convective-absolute transition with  $Fr \geq 1$  and  $\delta^2 \leq 3.5 \times 10^{-3}$ . Later they used a more sophisticated two-dimensional rotational model, i.e. Colombini's approach [26], setting  $\delta^2 \leq 10^{-3}$ . Fig. 3 shows that the critical curve for the onset of the absolute instability considered in our study (thick solid line) is in qualitative agreement with Vesipa et al. [77], see the thick dashed line.

The neutral curve of the convective-absolute transition for the onset of upstream migrating anti-dunes is derived herein using a spatio-temporal linear stability analysis in which the absolute nature of the instability is imposed algebraically through the zero group velocity condition [44,71]. The existence of saddle points has been corroborated geometrically by means of Briggs' or the cusp map method [48] though we do not report the details of this result for the sake of the brevity.

The dispersion relation of the temporal stability analysis given in Section 3.2 can be readily reused in the spatio-temporal stability study with the simple change of variables  $k = a$  and  $\omega = ac$ , where the spatial wavenumber  $k$  and the temporal frequency  $\omega$  are now both complex numbers. The phase velocity  $c_r = \omega_r/k_r$  of the erosion-deposition mode is negative, see the inset in Fig. 2(b), and consequently the bed perturbation moves upstream. Hence the base flow can be absolutely unstable if there is a saddle point  $k_0 \equiv k(\omega_0)$  with zero group velocity, i.e.  $c_g = \partial\omega/\partial k = 0$ , resulting from a pinch point between two spatial branches  $k(\omega)$  with  $k_{0,i} < 0$  (i.e. spatially growing solution) and  $\omega_{0,i} > 0$  (i.e. temporal growing solution). Similarly  $\omega_0 \equiv \omega(k_0)$  defines a branch point in the complex  $\omega$  plane. Branch points and pinch points satisfy the necessary condition

$$\mathbb{D}(k_0, \omega_0) = 0, \quad \frac{\partial \mathbb{D}}{\partial k}(k_0, \omega_0) = 0, \quad \frac{\partial^2 \mathbb{D}}{\partial k^2}(k_0, \omega_0) \neq 0, \quad (29)$$

ensuring  $c_g = \partial\omega/\partial k = (\partial\mathbb{D}/\partial k)/(\partial\mathbb{D}/\partial\omega) = 0$ . The two first equations in (29) were solved with the help of *Mathematica*.

We varied as control parameters  $Fr$  and  $\delta^2$  in the range of values shown in Fig. 3 with  $v_t = 0$  and find out the minimum value of the particle diffusivity  $\mathcal{D}$  required for the existence of solutions to (29) that are saddle points, see the result in Fig. 4(a). It is readily observed that the particle diffusivity  $\mathcal{D}$  plays a fundamental role in the convective-absolute transition as it should be larger than zero at all values of  $Fr$  and  $\delta^2$ . At a given grain-size to flow-depth ratio  $\delta^2$ , the minimum value of  $\mathcal{D}_{abs}$  is achieved at the lowest  $Fr$ , i.e. along the transition curve for the onset of anti-dunes (solid line in Figs. 3 and 4(a)). This critical value is depicted in Fig. 4(b) showing that the particle diffusivity grows with  $\delta^2$ . Then we proceeded ensuring the Briggs-Bers criterion by eye (geometric approach), as suggested by Juniper [47], by plotting contours of  $\omega_i$  in the  $k$ -space. Saddle points were pinched between branches  $k^+$  and  $k^-$  originated in distinct halves of the  $k$ -plane. Therefore our solution satisfies the Briggs-Bers criterion or Fainberg-Kurilko-Shapiro (Soviet literature) condition.

It is worth recalling that the wavelength of the most unstable mode can be adjusted by increasing the value of the non-dimensional eddy viscosity  $v_t$  as for the case already described in Fig. 2(d). In doing so one can ensure that the absolute wavelength lies in the range of experimental values  $0.3 \leq k_r \tan \theta \leq 2$  [e.g., [19,67]]. The wavelength selection mechanism observed in the full non-linear numerical simulation in Section 4.4 and the agreement between the anti-dunes wavelength obtained therein and experimentally by Mettra [62] serves to illustrate the absolute nature of the instability and the real capabilities of our modeling technique.

#### 4. Simulations

We present three numerical experiments in order to benchmark the numerical results against theoretical solutions. A brief description of the numerical scheme used in our simulations is given in Section 4.1. In the first set of simulations (Section 4.2) we consider a prescribed steady uniform flow and solve (5) for the continuous Poisson density  $b(x, t)$ . The numerical solutions are compared with the theoretical solutions built by Ancey et al. [3,4] and Heyman et al. [43] and with additional numerical simulations using simpler numerical schemes. Then, in Section 4.3, we focus attention on the deterministic part of the model equations. We start applying the linear stability

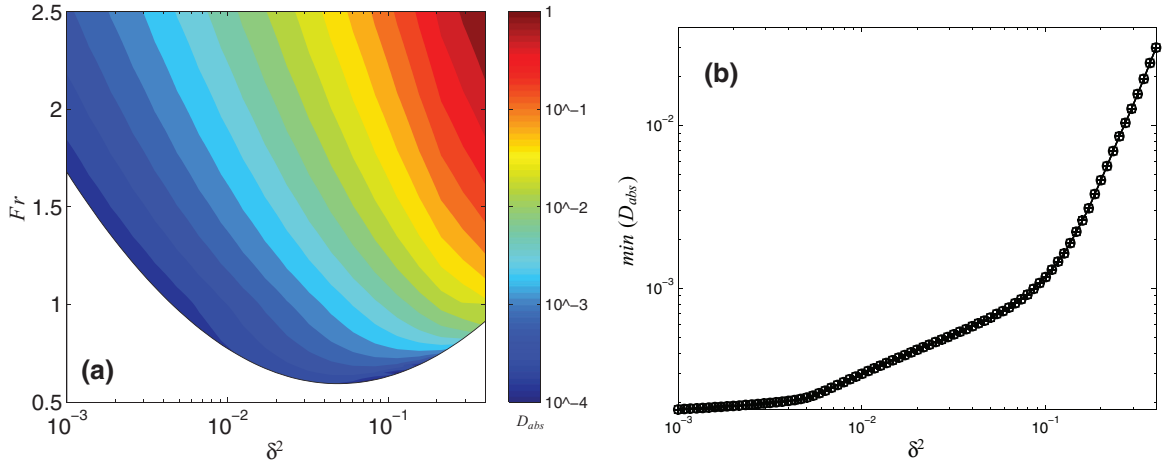


**Fig. 4.** (a) Minimum particle diffusivity  $D_{abs}$  required for the existence of saddle-points or an absolute instability and (b) plot of  $D_{abs}$  along the threshold condition depicted by the solid line in panel (a) and Fig. 3.

results of the mean balance equations (1)–(3) and (6) for a uniform flow down an erodible bed that allows us to evaluate the growth rate of infinitesimal disturbance from the linear dispersion relation. This result is subsequently used to verify the numerical growth rate of the full non-linear solution. Recall that we have found out that the model equations exhibit a richer collection of unstable modes than the classical Saint-Venant-Exner equations based on algebraic discharge equations. We conclude this section with additional simulations in Section 4.4 where we analyze the same scenario as in Section 4.3 and use the hybrid stochastic-deterministic equations on this occasion.

The main motivation to present the current set of numerical simulations is to illustrate the capabilities of our model for predicting noise-induced pattern formation, a problem that has always drawn the attention of the science community [69]. We have always found out the developments of anti-dunes, recall Fig. 3, and the existence of stochastic fluctuations in well-controlled laboratory experiments, as reported in [2,4,5,43]. Anti-dunes modify the bed slope and consequently affect the water flow conditions that, at the same time, alter the local bed load with respect to the equilibrium value under uniform flow conditions. Consequently, both anti-dunes and stochastic fluctuations provoke oscillations in the instantaneous bed load that is no longer steady, as observed in flume experiments. This article therefore contributes to improve the predictive capabilities of our model with respect to our previous theoretical works in which we did not consider the coupling with Saint-Venant equations. Furthermore, it represents an original contribution in the computation of noise-induced pattern formation.

#### 4.1. Numerical scheme

The non-linear set of balance laws (1)–(5) was recast in strong conservation form

$$\frac{\partial \mathbf{U}}{\partial t} + \frac{\partial \mathbf{F}}{\partial x}(\mathbf{U}) + \frac{\partial \mathbf{G}}{\partial x}(\mathbf{U}) = \mathbf{S}(x, \mathbf{U}), \quad (30)$$

$$\mathbf{U} = (h, h\bar{v}, b, y_b)^T, \quad (31)$$

$$\mathbf{F} = \left[ h\bar{v}, \frac{(h\bar{v})^2}{h} + \frac{gh^2}{2}, \beta\bar{v}b, 0 \right]^T,$$

$$\mathbf{G} = \left( 0, -\nu h \frac{\partial \bar{v}}{\partial x}, -D_u \frac{\partial b}{\partial x}, 0 \right)^T, \quad (32)$$

$$\mathbf{S} = \left[ 0, gy_b \frac{\partial y_s}{\partial x} + g \frac{\partial}{\partial x} \left( \frac{y_b^2}{2} - y_s y_b \right) - \frac{f}{8} \bar{v} |\bar{v}|, \right]$$

$$\left[ \lambda' - \kappa b + \xi_b \sqrt{2\mu b}, \frac{\kappa V_p B^{-1} \langle b \rangle - \lambda}{1 - \zeta_b} \right]^T, \quad (33)$$

and solved numerically in the computational domain  $0 \leq x \leq L$  made of  $m_x$  cells  $C_i = [x_{i-\frac{1}{2}}, x_{i+\frac{1}{2}}]$  with uniform size  $\Delta x = x_{i+\frac{1}{2}} - x_{i-\frac{1}{2}} = L/m_x$  ( $i = 1 \dots m_x$ ). We used the divergence form for bed slope source term in (33) to improve the numerical treatment of discontinuous bed profiles  $y_b$  with continuous free surface elevation  $y_s = y_b + h$  [16,74] which requires the evaluation of the streamwise gradient of the free surface instead of the bed elevation. The computational variables are  $\mathbf{U}_i^n$ , which approximate the average value over the  $i$ th interval at time  $t$ :

$$\mathbf{U}_i(t) \approx \frac{1}{\Delta x} \int_{C_i} \mathbf{U}(x, t) dx, \quad (34)$$

being located at the cell centroid  $x_i = (x_{i-\frac{1}{2}} + x_{i+\frac{1}{2}})/2$ . The influence of prescribed boundary conditions on the numerical results was avoided by setting a cyclic spatial domain with  $x_1 = x_{m_x}$ . The grid is consequently made only of interior cells. The high-order finite volume library SharpClaw [52,53] was employed as development environment. A fractional-step method was applied to split the advection-diffusion equations (30) into a hyperbolic subproblem with source terms and a parabolic subproblem [57]. The numerical strategy for the homogeneous hyperbolic system of equations is similar to the classical  $q$ -wave propagation algorithm that was adopted with success to compute roll wave developments for transient, non-uniform kinematic waves in previous contributions [13,15]. The innovative parts of the algorithm are introduced below, in particular the wave decomposition of the Riemann problem, the source term discretization and the summary of the full semidiscrete algorithm used in each time step, appropriate both for deterministic and stochastic partial differential equations [55]. The code was implemented in Fortran 2003, compiled with Intel® Fortran Composer XE for Linux and run in Fujitsu Celsius R920 with Intel® Xeon® CPU E5-2630 processors.

The resolution of the hyperbolic subproblem (non-diffusive part of the equations) was done in the first step of the algorithm given the numerical solution  $\mathbf{U}_i^n$  at the present instant of time  $t^n$ . Using a forward Euler scheme, the classical  $q$ -wave propagation algorithm reads [53,57]

$$\frac{\mathbf{U}_i^* - \mathbf{U}_i^n}{\Delta t} = -\frac{1}{\Delta x} \left( \mathcal{A}^- \Delta \mathbf{u}_{i+\frac{1}{2}} + \mathcal{A}^+ \Delta \mathbf{u}_{i-\frac{1}{2}} + \mathcal{A} \Delta \mathbf{u}_i \right) + \mathbf{S}_i. \quad (35)$$

Here  $\mathbf{U}_i^*$  represents the predicted value of the numerical unknowns at the new time step  $t^{n+1}$  in the absence of diffusion. The fluctuations

and the total fluctuation are evaluated at  $t_n$  as

$$\mathcal{A}^\pm \Delta \mathbf{u}_{i-\frac{1}{2}} = \sum_{p=1}^4 \left( s^p \left( \mathbf{u}_{i-\frac{1}{2}}^L, \mathbf{u}_{i-\frac{1}{2}}^R \right) \right)^p \mathcal{W}^p \left( \mathbf{u}_{i-\frac{1}{2}}^L, \mathbf{u}_{i-\frac{1}{2}}^R \right), \quad (36)$$

$$\mathcal{A}^\pm \Delta \mathbf{u}_i = \sum_{p=1}^4 \left( s^p \left( \mathbf{u}_{i-\frac{1}{2}}^R, \mathbf{u}_{i+\frac{1}{2}}^L \right) \right)^p \mathcal{W}^p \left( \mathbf{u}_{i-\frac{1}{2}}^R, \mathbf{u}_{i+\frac{1}{2}}^L \right), \quad (37)$$

which make use of the eigenvalues and eigenvectors associated with the Jacobian matrix of (30) described in Appendix A.

At this point it is worth highlighting that the inclusion of the bed load transport model tested in this paper does not alter the wave decomposition of the hydraulic subproblem. The eigenvalues, the eigenvectors and the Roe averages of the water phase unknowns ( $p = 1, 2$ ) coincide with the approximate Riemann solution of the Saint-Venant equations [40]. The two additional waves ( $p = 3, 4$ ) do not contribute to the fluctuations of the water depth nor the water discharge. The transition from subcritical to supercritical flow can be successfully reproduced using the same entropy fix method as for the shallow water equations. No modification is required by our model equations in contrast with coupled numerical methods based on the classical Exner equation (5) that run into difficulties in the presence of critical conditions [60]. Also the current Riemann solver can be employed to solve (5) for the mean particle concentration instead of equation (6) for the stochastic Poisson density, simply replacing  $b$  by  $\langle \gamma \rangle$  in (A.1)–(A.5).

The cell integral of the source terms  $\mathbf{S}_i$  in (33) is evaluated explicitly from the known solution at time  $t_n$ . The numerical integration of the momentum balance source terms was degraded to second order accuracy to be consistent with the discretization of the diffusive term described below. This implies that we evaluated the free-surface slope source term  $g v_b \partial_x y_s$  as described in LeVeque [58]. We computed the friction source term discretization by following Liang and Marche [59]. Furthermore the stochastic source terms were evaluated using the Euler–Maruyama scheme as in previous numerical studies using the finite difference method [1,3] and the finite volume method [7]. The ensuing method for the continuous Langevin equation corresponds to the Euler–Maruyama scheme and attains the strong order of convergence 0.5. Further details on the evaluation of the source terms are given in Appendix B.

Finally, the solution  $\mathbf{U}_i^*$  of the hyperbolic system of equations (35) was employed as guess value in the second step of the algorithm where we solve the parabolic subproblem. The eddy and particle diffusivity terms were integrated with the one-step implicit Crank–Nicholson scheme, which is second-order accurate in space and time,

$$\frac{\mathbf{U}^{n+1} - \mathbf{U}^*}{\Delta t} = \frac{1}{2} (\Psi(\mathbf{U}^*) + \Psi(\mathbf{U}^{n+1})), \quad (38)$$

with

$$\Psi(\mathbf{U}) = \frac{1}{\Delta x^2} \begin{pmatrix} 0 \\ h_{i-\frac{1}{2}} v_{i-\frac{1}{2}} \bar{v}_{i-1} - (h_{i-\frac{1}{2}} v_{i-\frac{1}{2}} + h_{i+\frac{1}{2}} v_{i+\frac{1}{2}}) \bar{v}_i + h_{i+\frac{1}{2}} v_{i+\frac{1}{2}} \bar{v}_{i+1} \\ D_u b_{i-1} - 2 D_u b_i + D_u b_{i+1} \\ 0 \end{pmatrix}. \quad (39)$$

This linear system of equations could be solved efficiently at each time step using Thomas algorithm for periodic tridiagonal systems without increasing substantially the computational cost nor decreasing the time step size [50]. The cell interface values in (39) were computed as the arithmetic average of the neighbor cells, e.g.  $h_{i-1/2} = (h_i + h_{i-1})/2$ . The implicit Crank–Nicholson scheme does not introduce any additional constraint on the time step  $\Delta t$ . In the field of  $\theta$ -methods for stochastic partial differential equations, one prefers

this scheme over explicit schemes such as the forward Euler method (which requires  $\Delta t \ll O(\Delta x^2/D_u)$ ) [41].

#### 4.2. The stochastic advection-diffusion Langevin equation

In this section, we compute the Poisson density  $b$  from (5) and benchmark the WENO scheme when the rest of variables  $\bar{v}$ ,  $h$ , and  $y_b$  remain constant. Detailed analytical solutions of the mean value, standard deviation, autocorrelation function and probability density function were presented by Ancey et al. [3]. Recall that for steady state problems, a random process is completely characterized by its autocorrelation and probability density functions. Other quantities such as moments, autocorrelation time, and energy spectrum can be inferred from these two functions.

Apart from the WENO schemes, standard finite difference methods are employed for the sake of comparison. In particular we used an implicit first-order upwind and pure second-order central scheme for the convective term together with Euler–Maruyama for the source term, as well as an explicit unlimited fifth order accurate central difference scheme together with the strong 1.5-order Taylor scheme [55], denoted by IUEM, ICEM and EXWP, respectively. The major interest of this benchmark is to check whether the WENO method reproduces the non-local effect induced by the convective operator in the presence of stochastic forcing, which is equivalent to increasing the particle diffusivity as outlined below. Recent numerical studies on this topic focused on finite differences, adaptive Discontinuous Galerkin method and Total Variation Diminishing finite volume methods for the stochastic Burgers equation [7,24,41] but little is known about the performance of the WENO scheme for the continuous version of the stochastic Langevin equation with advection. Before we start with the numerical simulations, two caveats are in order.

First, the numerical analysis of stochastic partial differential equations is an emerging field of research, which offers unexpected surprises. For instance numerical solutions to the stochastic Burgers equation (a nonlinear variant of the advection diffusion equation (5) studied here) highlight the influence of the mesh size on the solution to which the numerical schemes converge, a situation that contrasts with the deterministic case [41]. In the present context, Ancey et al. [3] showed that the advection diffusion equation (5) is derived by considering mass balance in finite volumes of control, then by taking the continuum limit. Yet, the process is random and furthermore it develops nonzero spatial cross correlations even under stationary homogeneous conditions. These spatial correlations give rise to scale-dependent diffusion-like effects. This means that even for particles moving at the same velocity ( $D_u = 0$ ), there is a dispersal induced by particle entrainment and deposition, which looks like particle diffusion (with a diffusivity  $\bar{u}_s \Delta x/2$ ) on the bulk scale. Thus the stochastic nature of the problem under investigation introduces effects that do not arise when studying deterministic advection diffusion equations.

Second, the statistical properties of the process studied depends on the spatial scale, so on the mesh size when we analyze them numerically. For this reason, we will distinguish between the sample variance of  $b$  (which is the variance of  $b(x, t)$  over a mesh of length  $\Delta x$ ) and the local theoretical variance inferred from (5). Ancey et al. [3] found that for a pure-advection problem, under steady state conditions, the mean Poisson density  $\langle b \rangle_{ss}$  and the sample variance  $\overline{\text{var}}_{ss} b$  are:

$$\begin{aligned} \langle b \rangle_{ss} &= \frac{\lambda'}{\kappa} \cdot \overline{\text{var}}_{ss} b \\ &\approx \frac{\mu \lambda' \Delta x^{-1}}{(\kappa + \bar{u}_s \Delta x^{-1})^2} \\ &\times \left[ 1 + \frac{\bar{u}_s \Delta x^{-1}}{\kappa + \bar{u}_s \Delta x^{-1}} + \frac{1}{2} \left( 3 - \frac{\lambda'}{\mu} \right) \frac{\bar{u}_s^2 \Delta x^{-2}}{(\kappa + \bar{u}_s \Delta x^{-1})^2} \right]. \quad (40) \end{aligned}$$

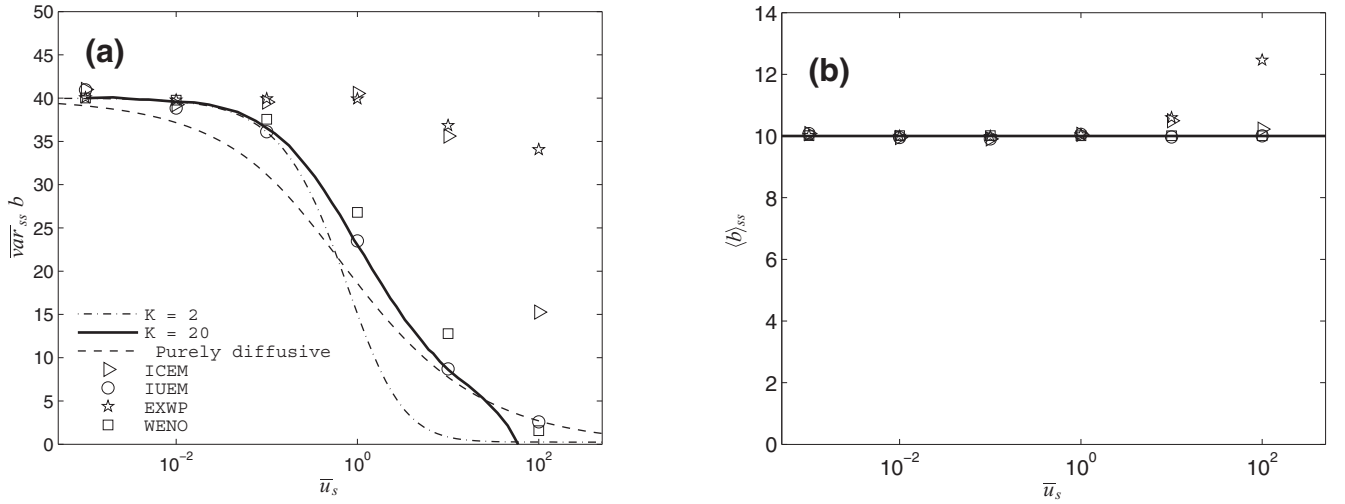


**Fig. 5.** (a) Steady-state sample variance  $\overline{\text{var}}_{ss} b$  and (b) mean value  $\langle b \rangle_{ss}$  as a function of the particle velocity  $\bar{u}_s$  with  $\lambda' = 10 \text{ m}^{-1} \text{ s}^{-1}$ ,  $\kappa = 1 \text{ s}^{-1}$  and  $\mu = 4 \text{ s}^{-1}$ . The dashed-dotted line and solid line represent the variance approximated to order 2 and 20, respectively. They are calculated iteratively from the cross correlations as described by Ancey et al. [3]. The dashed line is the variance (43) for a purely diffusive process [43] with  $D_u$  replaced with  $\bar{u}_s \Delta x / 2$ .

Here we just provide the second-order Taylor expansion of the variance. There is no closed form for the variance except for  $m x = 1$  [4], but it can be calculated iteratively. Guidelines to compute higher order corrections to  $\overline{\text{var}}_{ss} b$  can be found in [3]. The local variance derived from (5) is

$$\text{var}_{ss} b = \frac{\lambda' \mu}{\kappa}, \quad (41)$$

and is thus independent of the particle velocity  $\bar{u}_s$ . One may be surprised that the local variance is not affected by advection whereas the sample variance depends a great deal on it, but this odd behavior can be explained by the development of spatial cross correlations [3]. At leading order, the autocorrelation function is

$$\rho(t) = \exp(-(\kappa + \bar{u}_s \Delta x^{-1}) t) \quad (42)$$

and the probability density function is the gamma distribution  $Ga(\tilde{\alpha}, \tilde{\beta})$  with parameters  $\tilde{\alpha} = \langle b \rangle_{ss}^2 / \overline{\text{var}}_{ss} b$  and  $\tilde{\beta} = \overline{\text{var}}_{ss} b / \langle b \rangle_{ss}$ .

As the dispersal induced by entrainment and deposition looks like diffusion, it is interesting to determine the response system when the process is purely diffusive ( $\bar{u}_s = 0$  and  $D_u > 0$ ). In that case, Heyman et al. [43] and Ancey et al. [3] showed that the sample variance  $\overline{\text{var}}_{ss} b$  for a cell of length  $\Delta x$  is given by

$$\overline{\text{var}}_{ss} b = \text{var}_{ss} b \frac{2 l_c^2}{\Delta x^2} \left( \frac{\Delta x}{l_c} + \exp\left(-\frac{\Delta x}{l_c}\right) - 1 \right),$$

$$\text{var}_{ss} b = \frac{1}{2} \frac{\mu \langle b \rangle_{ss}}{\kappa} \frac{1}{l_c}, \quad l_c = \sqrt{\frac{D_u}{\kappa}}, \quad (43)$$

which approaches the steady-state value  $\text{var}_{ss} b$  in the limit  $\Delta x \rightarrow 0$ .  $l_c$  is the correlation length of diffusion.

Numerical simulations were performed with  $m x = 100$  cells of length  $\Delta x = 1 \text{ m}$  and the time step  $\Delta t = 0.001 \text{ s}$  during  $5 \times 10^5$  iterations. We explored the effect of varying the particle velocity  $\bar{u}_s$  from  $10^{-3}$  to  $10^2 \text{ m s}^{-1}$  setting  $D_u = 0$ ,  $\lambda' = 10 \text{ m}^{-1} \text{ s}^{-1}$ ,  $\kappa = 1 \text{ s}^{-1}$  and  $\mu = 4 \text{ s}^{-1}$ .

Fig. 5 (a) shows a comparison between the steady-state sample variance of the numerical solutions obtained from the WENO implementation vs. the first-order upwind (IUEM), the unlimited second-order (ICEM) and fifth-order (EXWP) central methods. Recall that IUEM and ICEM treat the convective and diffusive operators implicitly while WENO and EXWP are explicit in time. The analytical approximation (40) of the sample variance is represented by the dashed-dotted line while the solid line shows the higher-order approximation. We observe that the upwind scheme is in agreement with

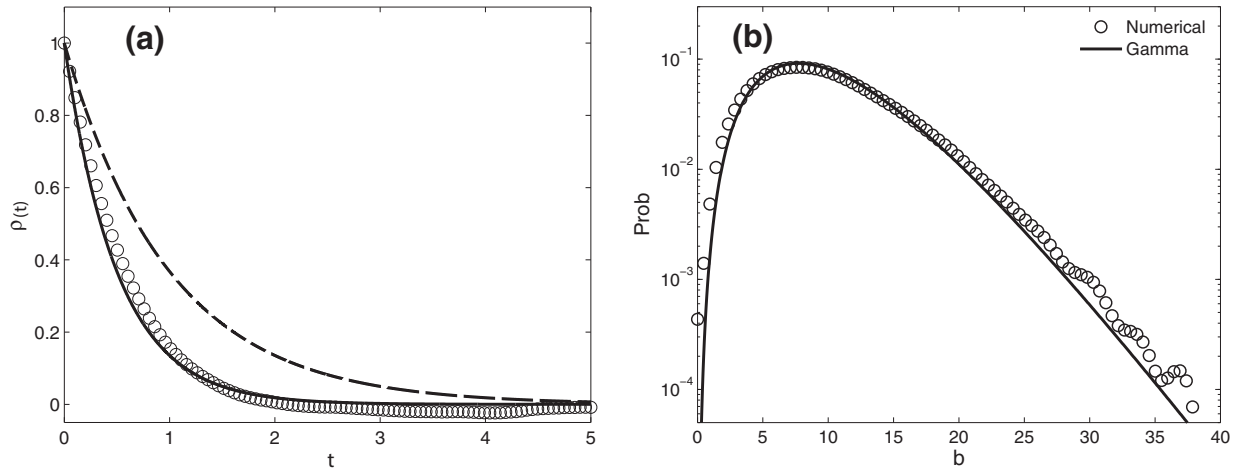
the higher-order analytical solution. The second-order approximation (40) holds for moderate values of  $\bar{u}_s$ , here when  $\bar{u}_s \leq 1 \text{ m s}^{-1}$  for the tested parameter values.

When increasing the sediment velocity  $\bar{u}_s$ , both the steady-state sample variance (40) and the numerical results go away from the theoretical local variance (41). As commented above, this deviation is explained by the development of positive spatial cross correlations, which significantly affects the sample variance. As the dispersal of particles takes the appearance of diffusion, it is very tempting to see whether a purely diffusive model is able to capture the trend shown by the numerical data. The dashed line in Fig. 5(a) shows the sample variance of a purely diffusive process for which the diffusivity is set to  $D_u \leftarrow \bar{u}_s \Delta x / 2$ . This curve provides a reasonably good approximation of the sample variance calculated theoretically (solid line) or computed using the upwind method (circles), which confirms the diffusion-like nature of the advection-induced dispersal. In contrast, the unlimited second-order and fifth-order central discretizations perform poorly because they are much less diffusive than the upwind and WENO solutions. This effect is readily observed in Fig. 5(a) for  $\bar{u}_s \geq 1 \text{ m s}^{-1}$  and is more evident in the EXWP method.

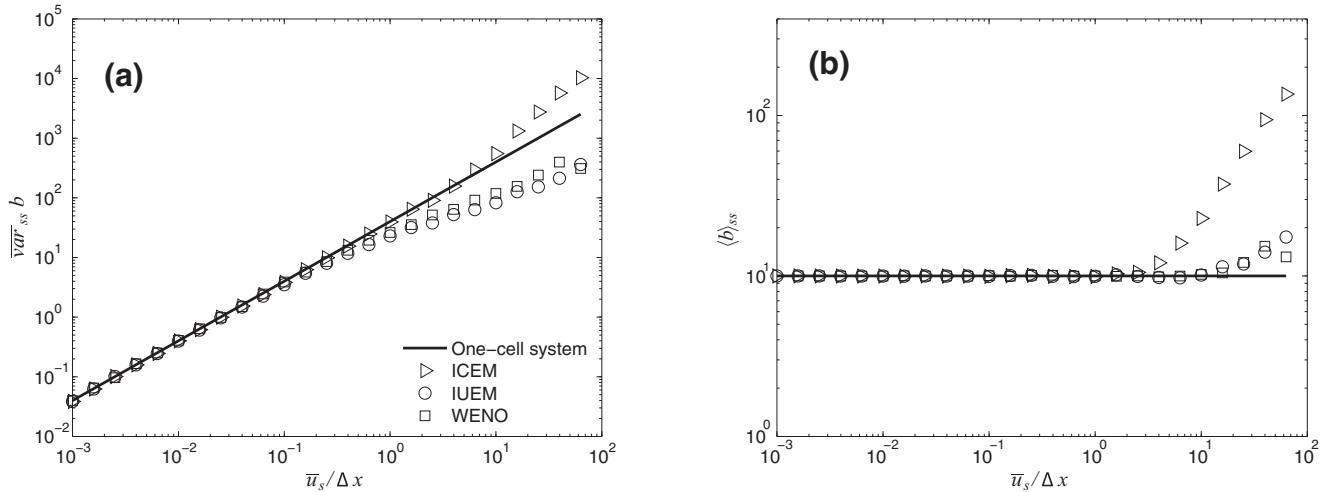
Fig. 5 (a) shows the steady-state mean  $\langle b \rangle_{ss}$  for completeness. Both the implicit upwind IUEM and the explicit WENO methods reproduce the constant analytical solution (40). It comes as no surprise that the WENO result lies close to the upwind one because the convergence rate is not greater than first order in the presence of discontinuous solutions [61]. The implicit second-order central scheme ICEM slightly overestimates the mean value for large velocities and the explicit unlimited high-order discretization EXWP diverges as we approach the Courant–Friedrich–Levy (CFL) stability condition. Note the large discrepancy between the mean value in EXWP and the exact solution at  $\bar{u}_s = 100 \text{ m s}^{-1}$ , i.e.  $\text{CFL} = \bar{u}_s \Delta t / \Delta x = 0.1$ . The error is triggered by the stochastic fluctuations and the unlimited high-order explicit treatment of the convective term. The explicit WENO scheme helps avoid such a drawback without requiring the implicit treatment of the convective term.

Fig. 6 shows the autocorrelation and probability density functions of the WENO data. The numerical data are closely matched by the analytical solution (42) and the gamma distribution  $Ga(\tilde{\alpha}, \tilde{\beta})$  with parameters  $\tilde{\alpha} = \langle b \rangle_{ss}^2 / \overline{\text{var}}_{ss} b$  and  $\tilde{\beta} = \overline{\text{var}}_{ss} b / \langle b \rangle_{ss}$ . These findings are similar to those previously reported with the explicit version of the upwind scheme [3].

An additional test was conducted to check the influence of the cell size on the numerical results. To this end we varied  $\Delta x$  between



**Fig. 6.** (a) Autocorrelation functions: the circles show the empirical autocorrelation function obtained from the numerical data (WENO scheme), the solid line corresponds to the theoretical solution (42) and the dashed line represents the same function but with  $\bar{u}_s$  set to zero. (b) Empirical probability distribution function of the Poisson rate  $b$  and the gamma distribution functions  $Ga$  with the input parameters given in Section 4.2. The probability density function of the continuous variable  $b(x, t)$  was computed in two steps: first the public software *cdf\_to\_pdf* written in Fortran by Bernd and Harris [12] was used to get the cumulative distribution function, then the result was differentiated using a symmetric finite difference formula of fifth-order accuracy. For both plots, we took  $\bar{u}_s = 1 \text{ m s}^{-1}$  in the numerical simulations. The impact of the sediment velocity  $\bar{u}_s$  on  $\rho(t)$  can be assessed by looking at the dashed line corresponding to  $\bar{u}_s = 0$ .



**Fig. 7.** (a) Steady-state sample variance  $\overline{\text{var}}_{ss} b$  and (b) mean value  $\langle b \rangle_{ss}$  as a function of the emigration rate  $\bar{u}_s/\Delta x$  with  $D_u = 0$ ,  $\lambda' = 10 \text{ m}^{-1} \text{ s}^{-1}$ ,  $\kappa = 1 \text{ s}^{-1}$ ,  $\mu = 4 \text{ s}^{-1}$  and  $\bar{u}_s = 1 \text{ m s}^{-1}$ . The solid line represents the steady-state variance and mean of the one-cell system given by (44) and Ancey et al. [4].

$10^{-2}$  and  $10^3 \text{ m}$ . The rest of parameter values were kept fixed relative to the previous simulation ( $\lambda' = 10 \text{ m}^{-1} \text{ s}^{-1}$ ,  $\kappa = 1 \text{ s}^{-1}$ ,  $\mu = 4 \text{ s}^{-1}$ ,  $\bar{u}_s = 1 \text{ m s}^{-1}$ ). In doing so, we expect to reach the mean Poisson density  $\langle b \rangle_{ss} = \lambda'/\kappa$  independently of the cell size  $\Delta x$  used in the simulation. For the sake of comparison with the theoretical results, the sample variance is plotted and compared with the sample variance calculated for one-cell systems ( $m\lambda = 1$ ). Ancey et al. [4] showed that for  $m\lambda = 1$  and steady-state conditions, the theoretical mean and sample variance are

$$\langle b \rangle_{ss} = \frac{\lambda'}{\kappa} = 10 \text{ m}^{-1}, \quad \overline{\text{var}}_{ss} b = \frac{\mu \lambda'}{\kappa} \frac{1}{\Delta x} = \frac{40}{\Delta x} \text{ m}^{-2}. \quad (44)$$

Fig. 7 shows the numerical mean and sample variance obtained with the explicit WENO, implicit upwind and implicit central schemes. The three numerical methods reproduce well the theoretical values of the one-cell system when the emigration rate is  $\bar{u}_s/\Delta x < 1 \text{ s}^{-1}$ . In contrast, the numerical values deviate from the theoretical results when  $\bar{u}_s/\Delta x > 1 \text{ s}^{-1}$ . The agreement between the theory and simulations is similar for both the mean [see Fig. 7(b)] and the sample variance [see Fig. 7(a)]. The central scheme significantly overestimates the steady-

state average  $\langle b \rangle_{ss}$ . The error associated with the WENO and upwind schemes are similar and much lower than with the central method. We can guarantee that the deviation between the numerical and theoretical solutions results from neither the time step  $\Delta t$  nor the corresponding CFL number because of the implicit treatment of the convective term in the IUEM scheme, which improves the stability compared to schemes. As a matter of fact we performed additional simulations with a time step one hundred times smaller and obtained the same result. The cause of this phenomenon is therefore related to the cell size  $\Delta x$  because the particle velocity  $\bar{u}_s$  was kept fixed in the simulations. We observe that there is a minimum cell size required to obtain realistic results in the simulations. The simple procedure used herein can be applied in general to establish the minimum grid length required in the numerical simulations for prescribed flow conditions.

Finally, a similar analysis of the influence of the window size  $\Delta x$  was used for a purely diffusive process with theoretical solution given by (43). The simulation parameters were the same as in the previous case except for the particle velocity, which was set to  $\bar{u}_s = 0$ , and the particle diffusivity, which is  $D_u = 0.2 \text{ m}^2 \text{ s}^{-1}$ . Fig. 8 shows the steady-state sample variance and the mean value as a function of the cell

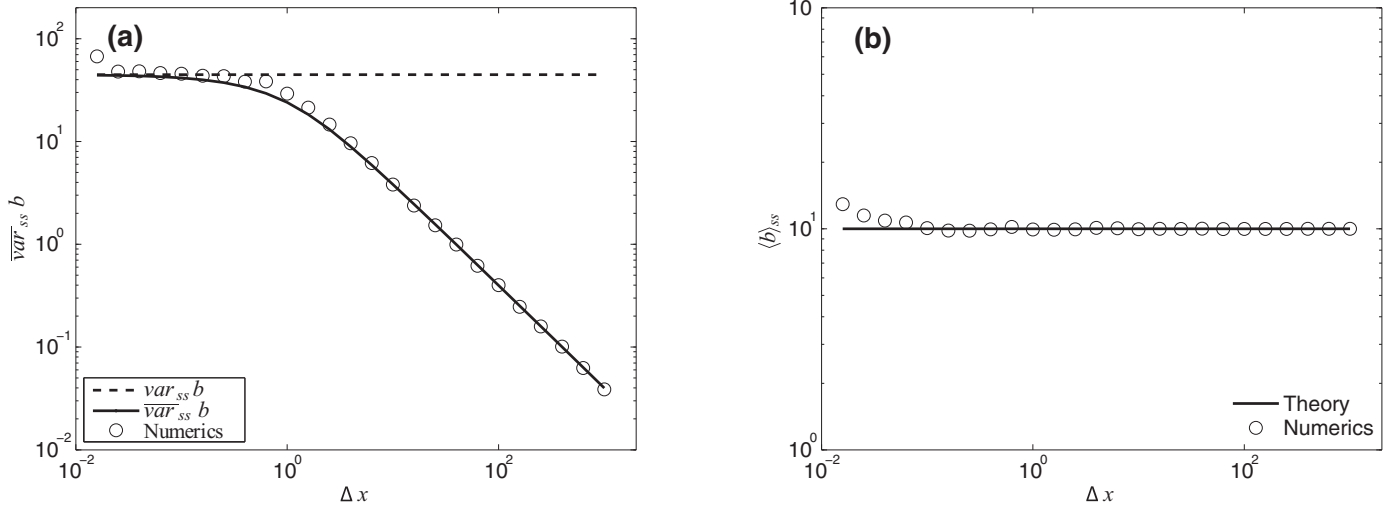


**Fig. 8.** (a) Steady-state sample variance  $\overline{\text{var}}_{ss} b$  and (b) mean value as a function of the cell size  $\Delta x$  for a purely diffusive process  $\bar{u}_s = 0$  with  $D_u = 0.2 \text{ m}^2 \text{ s}^{-1}$ ,  $\lambda' = 10 \text{ m}^{-1} \text{ s}^{-1}$ ,  $\kappa = 1 \text{ s}^{-1}$  and  $\mu = 4 \text{ s}^{-1}$ . The dashed line and the solid line in panel (a) represents the theoretical solution of the local, steady-state variance  $\text{var}_{ss} b$  and the sample variance  $\overline{\text{var}}_{ss} b$ , respectively, given by (43) and Heyman et al. [43]. Circles represent the numerical data.

size  $\Delta x$ . The dashed and solid lines in Fig. 8(a) correspond to the local variance  $\text{var}_{ss} b$  and the sample variance  $\overline{\text{var}}_{ss} b$  for a window of size  $\Delta x$ , both given by (43). The three solutions are nearly identical for small enough cell sizes  $\Delta x \ll 1 \text{ m}$ . However, the local variance deviates from the sample variance as  $\Delta x$  increases. The numerical solution matches the sample variance at all  $\Delta x$ , which highlights the performance of the numerical scheme. As shown by Fig. 8(b), agreement between theory and numerics for  $\langle b \rangle_{ss}$  is excellent for  $\Delta x > 0.1 \text{ m}$ .

The fluctuations described in the above set of numerical simulations are obviously due to the stochastic forcing  $\sqrt{2\mu b} \xi_b$  in the  $b$ -equation (5). We have verified that if the collective entrainment coefficient vanishes, i.e.  $\mu = 0$ , then the numerical solution preserves the equilibrium state  $b = \langle b \rangle_{ss}$  and does not exhibit spurious oscillations.

#### 4.3. The mean morphodynamic equations: pattern formation in the flow down an erodible slope

We have performed additional simulations with the coupled erosion-deposition model to verify the accuracy of the numerical scheme proposed in Section 4.1. First, we consider a steady uniform flow in the full mobility regime. This implies that the Shields numbers are much larger than the critical Shields number (in practice  $Sh > 2Sh_{cr}$ ) and the stochastic fluctuations are much lower than the mean value, i.e.  $(\text{var}_{ss} b)^{1/2} \ll \langle b \rangle_{ss}$ . We thus neglect the influence of the noise term  $\xi_b(x, t)$  in the  $b$ -equation (5). Classical deterministic bed load transport formulas  $\bar{q}_s(Sh)$  such as the ones proposed by Meyer-Peter & Mueller, Ashida & Michiue and Fernandez Luque & van Beek lead to the scaling  $\bar{q}_s \propto Sh^{3/2}$  under full sediment-mobility conditions [37]. As outlined in Section 2.2, an alternative approach to computing the sediment transport rate is to define it as  $\bar{q}_s = \bar{u}_s \langle \gamma \rangle - \partial_x (D_u \langle \gamma \rangle)$  [36] and then compute it using the mean equations (1)–(3) and (6). In Section 2.3, we showed how the entrainment and deposition rates could be determined from the experimental data provided by Fernandez Luque and van Beek [34]. We obtained expressions that are consistent with the erosion-deposition model by Charru [22] together with the numerical data obtained from direct simulations for Shields numbers as large as  $Sh \approx 4.3Sh_{cr}$  [32,56]. It can be shown that by considering the closure equations (13) and (15) together with the Darcy–Weisbach frictional law (8), we retrieve the power-law scaling  $\bar{q}_s \propto \tau_b^{3/2}$  because  $\tau_b \sim Sh$ . This provides clear evidence that the erosion-deposition model is also well-suited to describing the full mobility regime.

The linear stability results presented in Section 3 are now employed to verify the accuracy of the numerical scheme described in Section 4.1. We simulate the flow down an erodible slope inclined initially at an angle  $\theta = 2.75^\circ$  to the horizontal. The sediment size is  $d = 5.6 \text{ mm}$ . The water base flow, which is initially uniform and steady with the constant depth  $H = 1.4 \text{ cm}$  and the depth-averaged velocity  $V = 0.45 \text{ m/s}$ , is allowed to recirculate and carry sediment in a flume of length  $\Lambda = 0.2 \text{ m}$ . The initial condition at  $t = 0$  is the uniform equilibrium state  $h = H$ ,  $\bar{v} = V$  and  $\langle \gamma \rangle = \langle \gamma \rangle_{ss}$ , except for the bed elevation in which we introduce an infinitesimal sinusoidal disturbance of amplitude  $\epsilon = 10^{-7} \text{ m}$  in the form  $y_b(x, 0) = -x \tan \theta + \epsilon \sin(2\pi x / \Lambda)$ . The numerical computations were done with  $m_x = 100$  cells and the friction factor was kept constant,  $f = f(d/H)$  (9), during the numerical simulations so that we can compare the results with those predicted by linear theory. In the absence of detailed studies and calibration of the streamwise particle diffusivity, we set it to the arbitrary value  $D_u = 0.1 \text{ m}^2 \text{ s}^{-1}$ . The critical Shields number  $Sh_{cr}$  has been corrected locally during the numerical simulation with respect to the flat bed value  $Sh_{cr,0}$  as a function of the local bed slope using Cheshier’s method [e.g. 70]

$$Sh_{cr} = Sh_{cr,0} \max \left( \cos \theta - \frac{\sin \theta}{\tan \theta_0}, 0 \right) \quad (45)$$

in which the tangent of the static angle of response is  $\tan \theta_0 = 0.63$ .

The conditions of our virtual scenario mimic the experimental conditions used by Mettra [62] in his well-controlled laboratory experiments. He used a small-scale flume, in which only the water recirculated. A conveyor belt fed the flume with sediment at the desired rate. The flume length (2.5 m) was much larger than the computational domain (0.2 m) and allowed for the formation of nearly periodic anti-dunes. In Mettra’s experiments, the wavelengths and amplitudes of the largest anti-dunes were about 0.1–0.3 m and 0.01–0.02 m, respectively, and inspired our selection of the computational length and similar flow conditions.

We have performed two simulations by varying the non-dimensional eddy viscosity from  $\nu_t = 0$  to  $\nu_t = 10$ . The first one allows us to compare the numerical growth rate of an infinitesimal disturbance with the prediction by the linear theory given by the dispersion relation (27). The non-dimensional wavenumber corresponding to the cyclic flume length is  $a = 2\pi H / (\Lambda \tan \theta) = 9.3641$ . The second scenario is more realistic because the model equations include a simplified version of the eddy viscosity, which has been

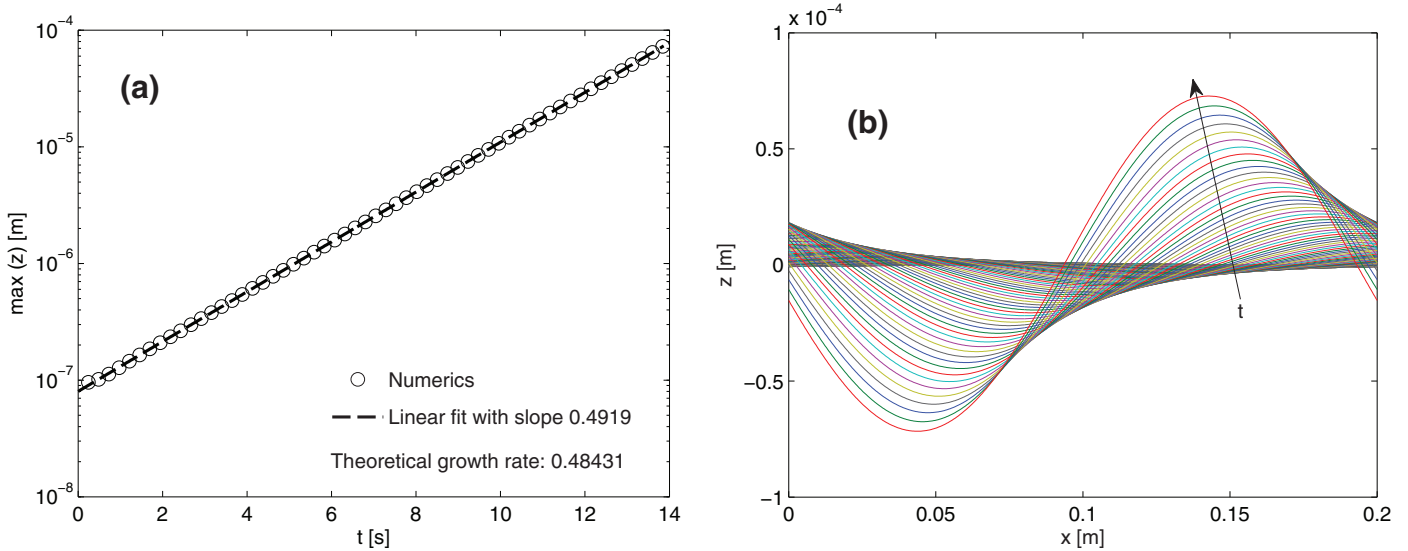


**Fig. 9.** Non-linear numerical simulation of the growth of infinitesimal perturbations with initial amplitude in the bed elevation of  $10^{-7}$  m: (a) maximum amplitude of the bed elevation perturbation as a function of time, (b) streamwise profiles of the bed elevation perturbation (flow is from left to right). A periodic flume inclined initially at an angle  $\theta = 2.75^\circ$  with grain size of  $d = 0.0056$  m and uniform base flow of depth  $H = 0.014$  m is used as base flow. The particle and turbulent diffusivity are set to  $D_t = 0.1 \text{ m}^2 \text{ s}^{-1}$  and  $\nu_t = 0$ , respectively. The non-dimensional parameters pertaining to the background flow are  $\delta^2 = 0.4$ ,  $Fr = 1.20$ ,  $T = 1.43$ ,  $\beta = 1$ ,  $\mathcal{D} = 0.74$ ,  $f = 0.27$ ,  $k_e = 8.64 \times 10^{-2}$  and  $k_d = 4.52$ , which leads to the non-dimensional growth rate  $a_{c_i} = 0.32248$  by solving the dispersion relation (27) with the non-dimensional wavenumber  $a = 9.3641$ . The dimensional growth rate  $0.48686 \text{ s}^{-1}$  is obtained by scaling the previous result with the factor  $V \tan \theta / H$ , see Eq. (21). The relative error of the numerical growth rate 1.03% is negligible.

proven necessary to simulate hydrodynamic instabilities such as roll waves [18] and cyclic steps [11]. The non-dimensional parameters required as input data by the stability analysis are  $\delta^2 = 0.4$ ,  $Fr = 1.20$ ,  $T = 1.43$ ,  $\beta = 1$ ,  $\mathcal{D} = 0.74$ ,  $f = 0.27$ ,  $k_e = 8.64 \times 10^{-2}$ ,  $k_d = 4.52$  and  $\nu = 0.125$ . Note that the transport stage number is quite high  $T > 1$ , which indicates that experiments were conducted under full mobility conditions ( $Sh > 2Sh_{cr}$ ). The ideal and viscous linear growth rates obtained from the linear stability theory are  $a_{c_i} = 0.32248$  and  $0.045328$ , respectively. Interestingly we found out that the linear theory predicts the development of the erosion-deposition instability in both situations. There is only one unstable eigenvalue that indicates that roll waves are not plausible. Indeed, the Froude number  $Fr = 1.2$  lies below the critical value of  $\sim 2$ . The dimensional growth rates of the erosion-deposition instability are obtained by scaling the previous result with the factor  $V \tan \theta / H$  leading to  $0.48686$  and  $0.06843 \text{ s}^{-1}$ . As expected the eddy viscosity stabilizes the perturbations by decreasing the growth rates of unstable perturbations.

Fig. 9 shows details of the early linear stage of the growing perturbation with  $\nu_t = 0$ . The temporal evolution of the amplitude of the bed elevation perturbation is shown in panel (a) in which the linear regression gives a numerical growth rate of  $0.4919 \text{ s}^{-1}$  that lies really close to the exact solution  $0.4869 \text{ s}^{-1}$ . The relative error 1% is indeed small. Fig. 9(b) illustrates the pattern formation (with the water flowing from left to right) as time progresses. The initial sinusoidal perturbation grows upstream as observed in the displacement of the stoss side. The inclusion of the non-dimensional eddy diffusivity  $\nu_t = 10$  in the model did not change the unstable behavior in the early stage, as shown in Fig. 10. The agreement between the linear theory and the numerics is once again good. The growing wavelength in the simulations shown in Figs. 9 and 10 corresponds in both cases with the wavelength of the sinusoidal disturbance introduced as initial condition. During the growth of the physical disturbance we did not observe shorter wavelengths nor spurious oscillations. The numerical growth rate  $0.06785 \text{ s}^{-1}$  [see Fig. 10(a)] agrees well with the theoretical solution  $0.06843 \text{ s}^{-1}$ . The relative error is only 0.85%, which shows the accuracy of the numerical scheme. The contours of constant  $z$  in Fig. 10(b), where  $z$  denotes the bed elevation perturbation obtained in the numerical simulation, readily show that the characteristic curves

travel in the upstream direction as the water flows towards  $x > 0$  (downstream direction). Therefore the bed form corresponds to an anti-dune. The bed perturbation elevation reaches a saturated state at late time ( $t \approx 160$  s) when the anti-dune amplitude is  $0.025$  m—this is same order of magnitude as found out in the experiments run by Mettra [62]. A snapshot of the solution is plotted in Fig. 10(c) and (d) where the bed elevation  $y_b$ , the free-surface elevation  $y_s$  and the Froude number are shown at  $t = 0$  (dashed lines) and  $t = 160$  s (solid lines). The bed development of the anti-dune has substantially modified the uniform flow condition used as base flow at the initial instant of time. The flow is no longer uniform. The bed morphology and flow dynamics resemble that observed with bed forms under supercritical flow conditions (anti-dunes, steep-pools and cyclic-steps), notably characterized by substantial time variations of the Froude number [20]. Indeed the Froude number value that was initially 1.2 varies progressively at later times from 0.91 to 2.22 as the water flows on the anti-dune. Note that the critical flow conditions  $Fr = 1$  (with transitions from subcritical to supercritical flow and viceversa) are resolved without further difficulty compared to the inviscid shallow water equations.

So far we found out that the mean equations (1)–(3) and (6) are unstable because of the development of an erosion-deposition instability even at subcritical Froude numbers, see Fig. 2. The linear stability theory correctly predicts the growth rate values that are not affected by non-linear effects during the growth of unstable perturbations, see Figs. 9 and 10. When based on algebraic sediment discharge equations  $\bar{q}_s(Sh)$ , the Saint-Venant-Exner equations (1)–(2) and (5) are stable for  $Fr < 2$  [10]. In contrast, the current model exhibits a richer collection of unstable modes particularly for  $Fr_{ed} < Fr < 2$ , similar to other one-dimensional formulations recently proposed [11,76]. More sophisticated rotational two-dimensional flow models have been suggested in the context of longitudinal bed forms for subcritical and supercritical regimes [e.g. [35,28,17]]. The one-dimensional deposition-entrainment shallow water formulations proposed here might be a valuable alternative to conduct further studies on pattern formation, particularly because of its simplicity and because it makes it possible to update previous numerical codes for Saint-Venant equations.

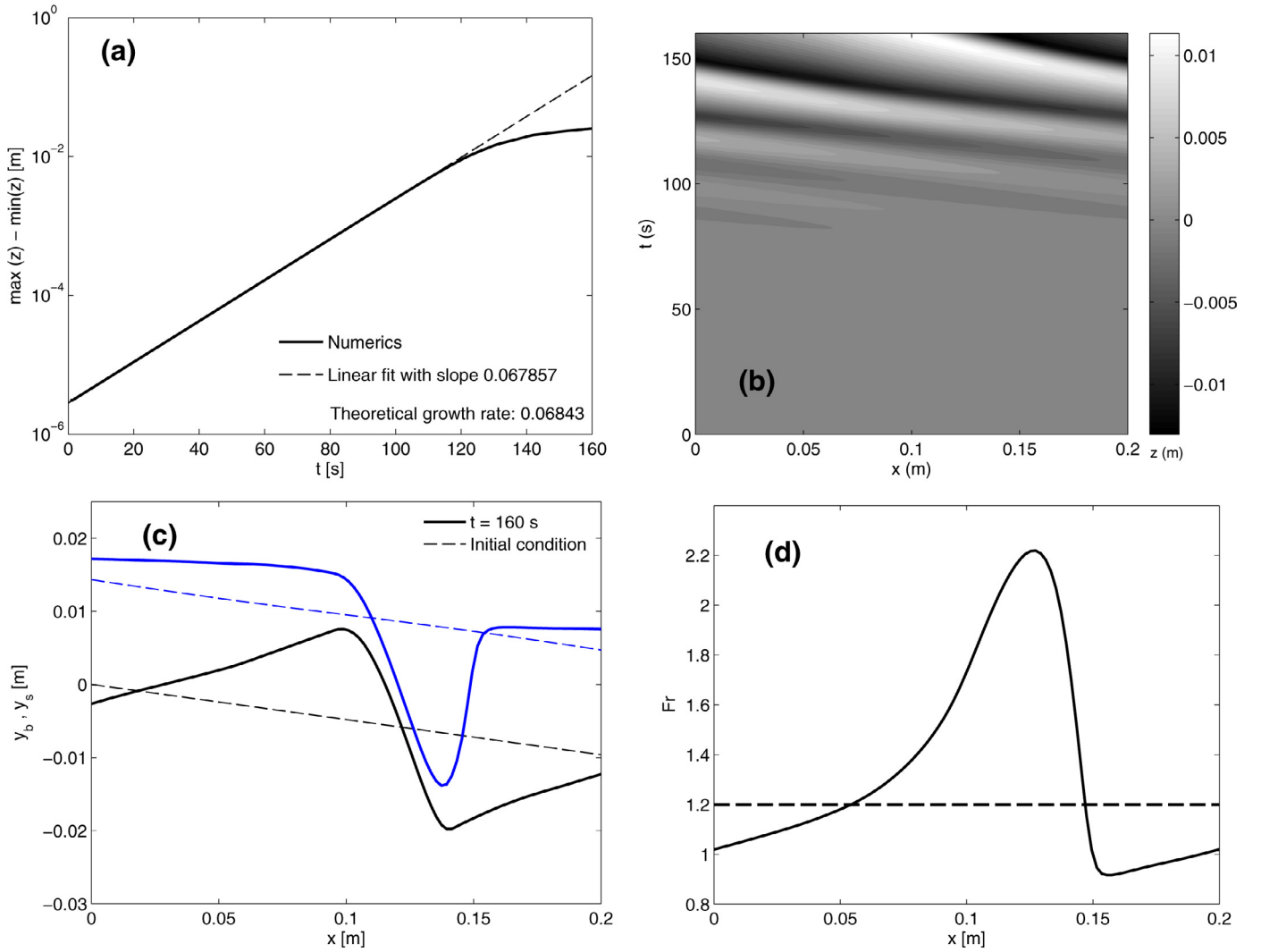


**Fig. 10.** Numerical results obtained with the mean flow equations for the same base flow conditions as used in Fig. 9 after increasing the eddy diffusivity coefficient up to  $\nu_t = 10$ : (a) temporal evolution of the amplitude of the bed elevation perturbation  $z$ , (b) contour plot of the bed elevation perturbation  $z(x, t)$ , (c) streamwise profiles of the bed elevation (in black) and free surface (in blue) at the initial time and at  $t = 160$  s, and (d) Froude number at the same times. The characteristic curves in panel (b) travel upstream, which shows that the bedforms corresponds to anti-dunes. (For interpretation of the references to color in this figure legend, the reader is referred to the web version of this article.)

#### 4.4. The hybrid stochastic-deterministic model

In this section we present numerical results obtained with the hybrid stochastic-deterministic model (1)–(5) for the same flow conditions and values of the physical parameters as in the deterministic simulations presented in Section 4.3. The only differences were the flume length, flume width, cell size and time step, which were of 3.5 m,  $\Delta x = 0.01$  m,  $B = 0.08$  m, and  $\Delta t = 2.2 \times 10^{-4}$  s (CFL = 0.01), respectively. The individual entrainment rate  $\lambda_i$  in (5) is evaluated using (B.3), which yields  $\lambda_i = 969.84 \text{ m}^{-1} \text{ s}^{-1}$ . In the absence of detailed studies on individual and collective entrainment of particles, the differential rate between deposition and collective entrainment rates is set to the constant value  $\kappa = 5.31 \text{ s}^{-1}$  given by (16) while the collective entrainment is fixed to  $\mu = 24.53 \text{ s}^{-1}$ . By assuming that the particle diffusivity controls the stochastic fluctuations of  $b$  (43), the fluctuation amplitude is about  $\pm(\overline{\text{var}} b)^{1/2}/\langle b \rangle_{ss} \times 100 = \pm 30\%$ . As initial conditions we consider a perfectly uniform flow down an inclined plane of constant slope.

Fig. 11 (a) shows the maximum amplitude of the bed elevation perturbation  $z$  as a function of time. Three phases are distinguished since the early development of the stochastic process: the growth of infinitesimal trains of disturbances in the bed (phase I with  $t \leq$

1800 s), the exponential growth of bed forms with a selected wavelength (phase II with  $1800 \leq t \leq 5000$  s) and the development of a saturation stage at  $t > 5000$  s (phase III).

At the intermediate time  $t = 1800$  s the flow looks like the perfect uniform flow used as initial condition [see Fig. 11(b)] because the amplitude of the bed elevation is negligible [ $< 10^{-3}$  m, see also Fig. 11(c)]. However there are wide fluctuations in the Poisson density  $b$  during the whole phase I, as revealed by the dashed line in Fig. 11(d) at that time. Indeed, the mean value  $\langle b \rangle$  and the sample variance  $\overline{\text{var}} b$ , which were computed every  $5 \times 10^4$  iterations, lie really close to the values of the purely diffusive process (43) with  $\langle b \rangle_{ss} = 182.54 \text{ m}^{-1}$  and  $\overline{\text{var}}_{ss} b = 3000 \text{ m}^{-2}$ , see Fig. 12. Here the sample variance approaches the local steady-state variance  $\text{var}_{ss} b = 3072 \text{ m}^{-2}$  due to the small grid size  $\Delta x$  used in the numerical simulation (recall the results in Fig. 8). The extra diffusivity induced by the convective term  $\bar{u}_s \Delta x / 2 = 0.002 \text{ m}^2 \text{ s}^{-1}$  is much smaller than the particle diffusivity  $D_u = 0.1 \text{ m}^2 \text{ s}^{-1}$  employed in the computations and, consequently, its effect is negligible. The autocorrelation function  $\rho(t)$  and the probability distribution function agree very well with the theoretical solutions for the diffusive process, as shown in Figs. 12(c) and 12(d) at the early instants of time  $t < 180$  s.

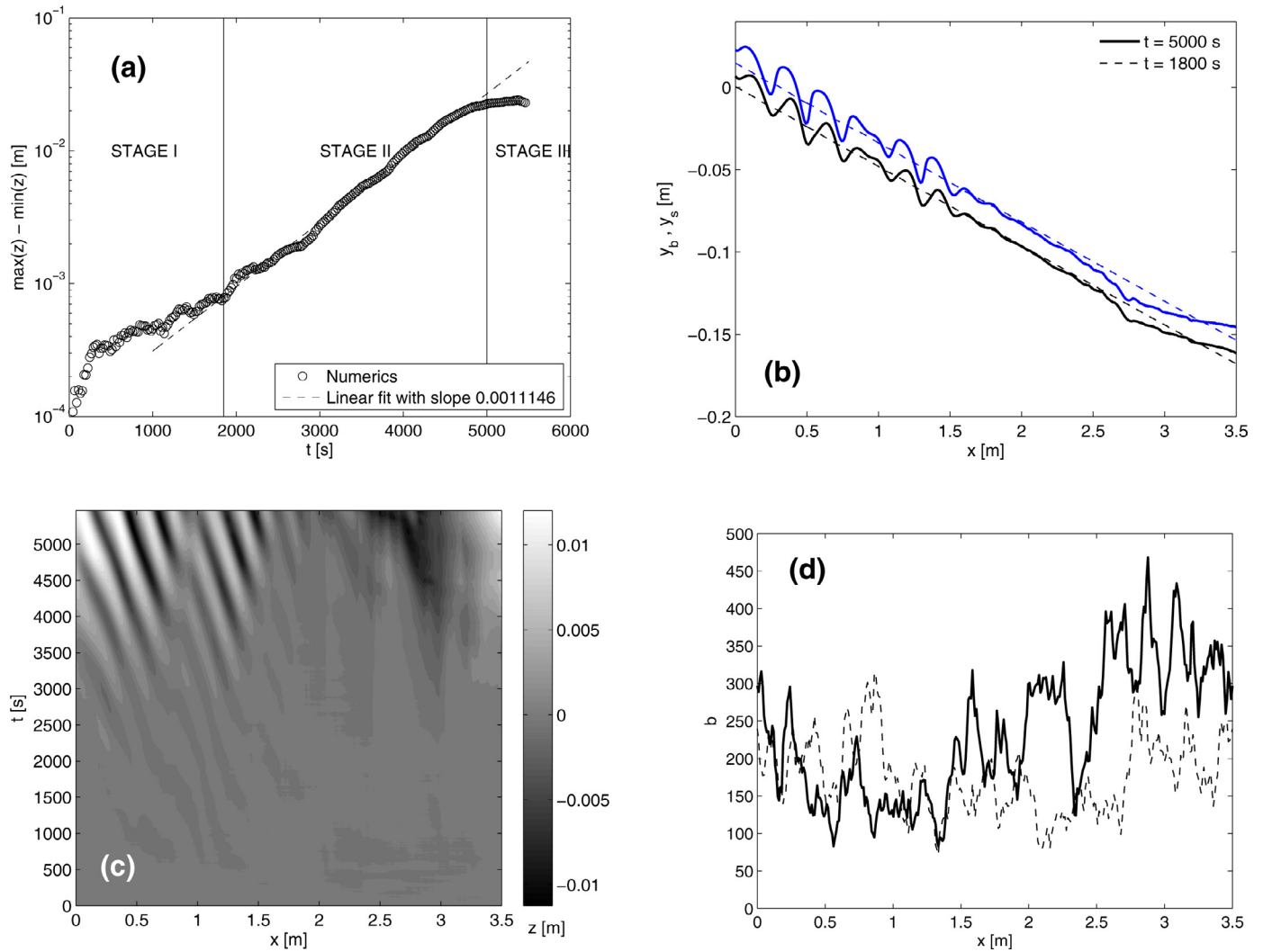


**Fig. 11.** Numerical results obtained with the stochastic model (1)–(5) for the same base flow conditions as used in Fig. 10 and  $\mu = 3 \text{ s}^{-1}$ : (a) temporal evolution of the amplitude of the bed elevation perturbation  $z$ , (b) streamwise profiles of the bed elevation (in black) and free surface (in blue) at the intermediate time  $t = 1800 \text{ s}$  and under steady-state conditions at  $t = 5000 \text{ s}$ , (c) contour plot of the bed elevation perturbation  $z(x, t)$  and (d) Poisson rate at the same instants of time as in panel (b). The characteristic curves in (b) travels upstream indicating that the bedforms corresponds with anti-dunes. (For interpretation of the references to color in this figure legend, the reader is referred to the web version of this article.)

The second phase is characterized by the exponential growth of anti-dune trains in the subregion  $x < 1.7 \text{ m}$ . The wavelength is well defined, varies in the  $0.22 \leq \Lambda \leq 0.29 \text{ m}$  range and remains nearly constant until it reaches the non-linear steady state, as commented in Section 4.3 for the single anti-dune simulation. The final amplitudes of the bed forms agree well with the previous one obtained in the pure deterministic simulation. This is not surprising as the wavelength employed in the deterministic simulation is close to the natural one determined for the stochastic case. In this simulation the wavelength of the bed forms is not imposed but is selected naturally in the simulations. However, in the stochastic simulation the growth rate inferred from the linear fit performed in Fig. 11(a) is much smaller than the one obtained in the deterministic case,  $0.001$  vs.  $0.068 \text{ s}^{-1}$ . The wide stochastic fluctuations affect the growth of small amplitude waves by attenuating their growth rates, but do not impeded their development.

The wavelength developing in the numerical simulation is in good agreement with the most unstable wavenumber obtained in the temporal stability analysis. Solving the dispersion relation of (26) with  $\delta^2 = 0.4$ ,  $Fr = 1.2$ ,  $u_* = 0.64$ ,  $\beta = 1$ ,  $\mathcal{D} = 0.74$ ,  $\nu = 0.13$ ,  $f = 0.27$ ,  $k_e = 8.64 \times 10^{-2}$  and  $k_d = 4.52$  for different values of  $a$ , and plotting the temporal growth rate as we did in Fig. 2(d), we found out the

most unstable dimensionless wavenumber:  $a \tan \theta = 2\pi H/\Lambda = 0.3$ . This value agrees well with those associated with the wavelengths of the numerical simulation  $0.3 \leq 2\pi H/\Lambda \leq 0.4$ . Furthermore, it lies really close to the experimental values  $0.25 \leq 2\pi H/\Lambda \leq 0.3$  by Mettra [62], see his Fig. 6.13, corresponding with the experiences marked in the  $\{Fr, \delta^2\}$  diagram in our Fig. 3. Indeed the flow conditions simulated herein mimics his experience 4deg3v, see Table 4.1 in [62]. This fact provides a further experimental validation of our theory and simulations.

The sedimentary dynamics in the lower reach of the flume are different while the bed remains nearly flat in the middle reach ( $1.7 < x < 2.5 \text{ m}$ ), shows degradation upstream ( $2.5 < x < 3.2 \text{ m}$ ) and aggradation downstream ( $x > 3.2 \text{ m}$ ). Part of the released sediment is deposited in the bed forms where sediments accumulate. The amount of extra sediment in the bed has been evaluated as  $\sum_i z(x_i, t)/mx = \sum_i (y_b(x_i, t) - y_b(x_i, 0))/mx$  in order to quantify the local mass error introduced by the noise term  $\xi_b$ . Fig. 13 shows that the cumulative volume of extra sediment in the computational cells is really small ( $< 2 \times 10^{-4} \text{ m}$ ). The artificial creation and destruction of sediment mass can be consequently neglected.

To conclude, it is worth mentioning that the empirical mean and variance shown in Fig. 12 are close to the steady-state values during

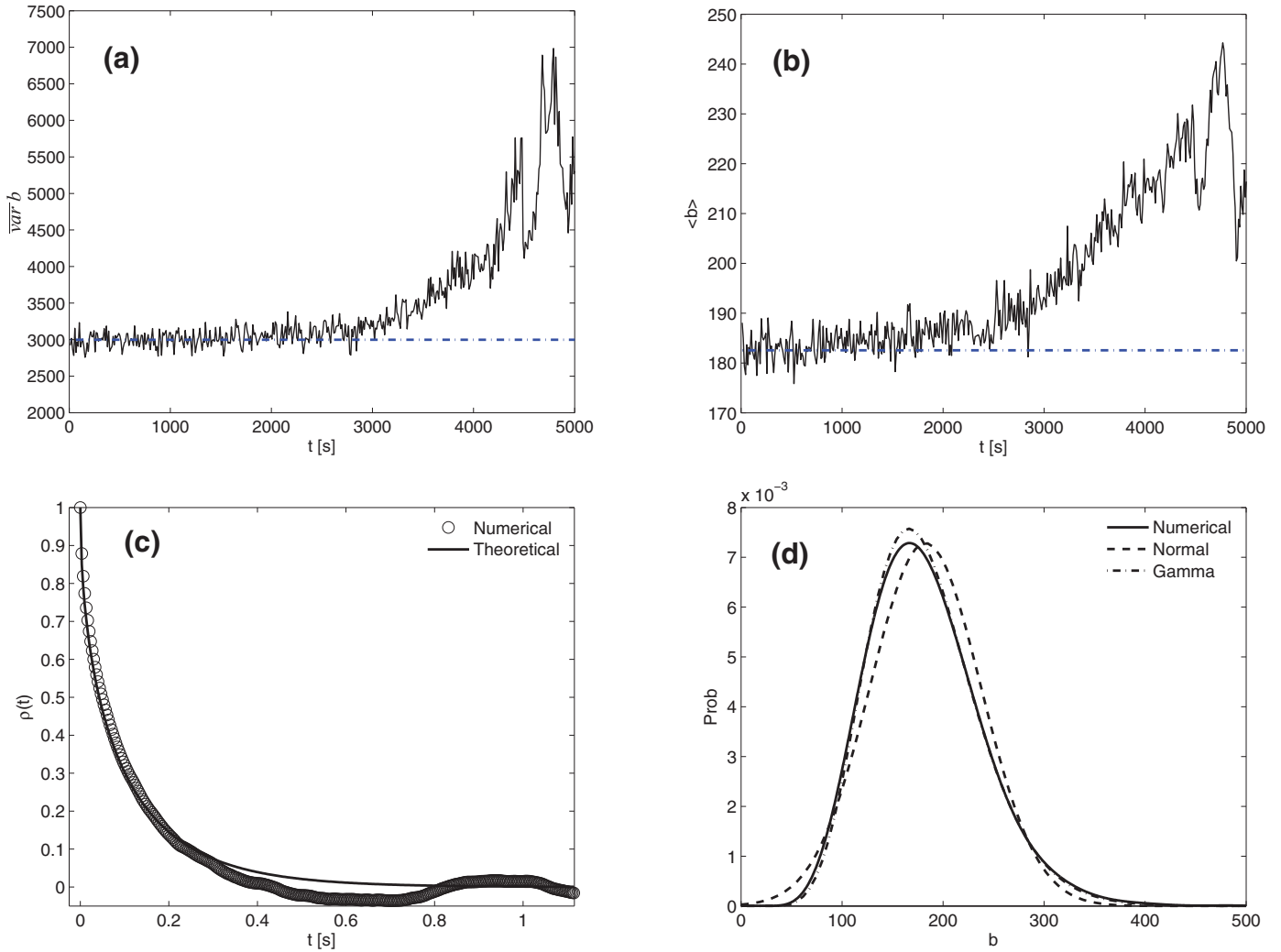


**Fig. 12.** (a) Empirical variance and (b) mean value computed every  $5 \times 10^4$  iterations (solid line) for the simulation shown in Fig. 11. The dashed line corresponds to the theoretical values of the diffusive process (43). (c) Autocorrelation functions: the circles show the empirical autocorrelation function obtained in the time interval  $t \leq 180$  s, the solid line corresponds to the theoretical solution  $\rho(t) = 1 - \text{erf}(\sqrt{\kappa} t)$ . (d) Empirical probability distribution function of the Poisson density  $b$  computed for  $t \leq 180$  s, the normal distribution function with mean  $\langle b \rangle_{ss} = 182.54 \text{ m}^{-1}$  and variance  $\overline{\text{var}}_{ss} b = 3000 \text{ m}^{-2}$ , and the gamma distribution function with input parameters  $\tilde{\alpha} = \langle b \rangle_{ss}^2 / \overline{\text{var}}_{ss} b = 11.11$  and  $\tilde{\beta} = \overline{\text{var}}_{ss} b / \langle b \rangle_{ss} = 16.43 \text{ m}^{-1}$ .

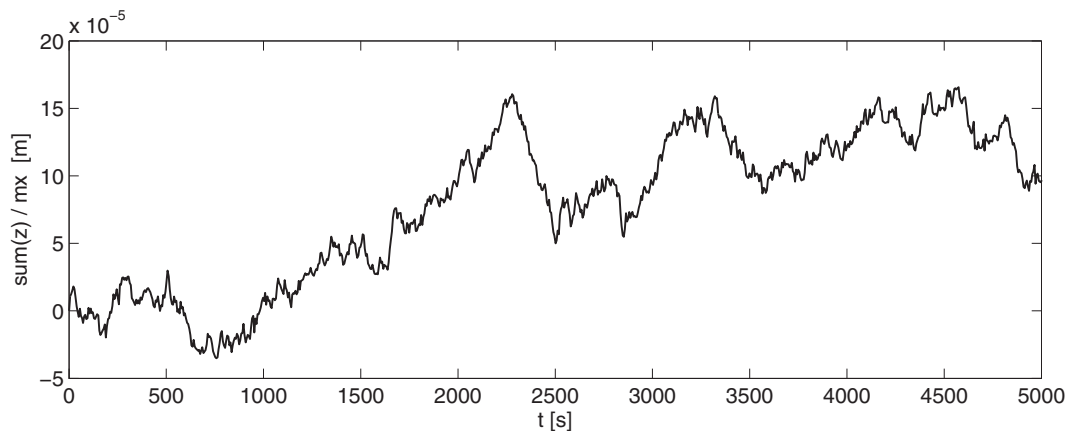


**Fig. 13.** Evaluation of the local cumulative error induced by the noise term  $\xi_b$  in the volume of sediment available in the bed as  $\sum_i z(x_i, t) / mx = \sum_i (y_b(x_i, t) - y_b(x_i, 0)) / mx$ .

the period of time  $t \leq 2500$  s when the amplitude of the bed forms were small. Later the flow becomes non-uniform and, consequently, the variance and the mean deviate from the equilibrium values and reach a maximum, of  $6985 \text{ m}^{-2}$  and  $244.3 \text{ m}^{-1}$ , respectively, at a later time  $t \approx 4790$  s. It seems important to take into account the non-uniformity of the flow field when evaluating the Poisson density  $b$ . Fig. 11(d) indeed shows larger fluctuations in the streamwise profile of  $b$  at  $t = 5000$  s compared to  $t = 1800$  s. The numerical model developed in this work allows for this task and could be useful to calibrate the model parameters from flume experiments.

## 5. Summary and conclusions

In this article we have proposed a stochastic bed load transport model (1)–(5) within the framework of the frictional shallow-water equations. To our knowledge, this is the first attempt of resolution of the stochastic-deterministic Saint-Venant-Exner equations. A potential application is the study of noise-induced pattern formation which has been considered in detail through the current article. The original experiments by Gilbert in 1914 [39] and subsequent studies [e.g., [20,51,62,67]] showed the developments of pattern formation on background flows that are essentially a uniform stream down an erodible bottom slope. We have considered the particular case of anti-dunes formation in steep slopes occurring for threshold Froude numbers approximately of 0.5–1.8 [19] and have proven by means of a spatio-temporal linear stability analysis that the unstable modes of our mean balance equations (20) correctly catch the anti-dune regime depicted in Fig. 3. We found out a minimum particle diffusivity  $\mathcal{D}_{abs}$  required for the onset of anti-dunes, see Fig. 4(a), corroborating that pattern formation is a diffusive process as in Turing-like instabilities [69]. The wavelength selection mechanism observed in the full non-linear numerical simulation in Section 4.4 and the agreement between the anti-dunes wavelength obtained therein with the absolute instability theory and the experiments by Mettra [62] serves to illustrate the potential capabilities of our modeling technique.

In the absence of collective entrainment, i.e.  $\mu = 0$ , and uniform flow conditions, our model retrieves the bed load flux function  $\bar{q}_s$  by Fernandez Luque and van Beek [34] which could be readily extended with further classical bed load formulas for calibration in the near future. In addition, the current stochastic formulation comprises a parabolic subproblem and a Wiener process representing physical processes as diffusive sediment transport and stochastic fluctuations. Hence the numerical method developed to solve the model equations (1)–(5) includes not only an approximate Riemann solver for the hyperbolic subproblem but also a Crank–Nicholson scheme combined with the Euler–Maruyama method for the stochastic source terms. The simulations presented in the numerical analysis in Section 4 have shown that the proposed numerical scheme allows us to accurately compute the statistical properties of the Poisson density  $b$  such as the mean, sample variance, autocorrelation function and probability density function. Furthermore the dimensions of the anti-dunes obtained in the full non-linear numerical simulation are physically sound and lie in the range observed in laboratory experiments. The current numerical model could be valuable to calibrate the input parameters from experimental or field data and could be readily incorporated in other source codes previously developed for the Saint-Venant equations.

## Acknowledgments

Bohorquez acknowledges the financial support by École Polytechnique Fédérale de Lausanne and Junta de Andalucía (research stays 2012–2014), CEACTierra (project #2013/00065/001), the Caja Rural Provincial de Jaén and the University of Jaén (project #UJA2014/07/04). Christophe Ancey was supported by the Swiss National Science Foundation under grant no. 200021–129538 and

200021–160083 (projects called “The Stochastic Torrent: stochastic model for bed load transport on steep slope”). The Authors thank Carlo Camporeale and Javier Murillo for their constructive and valuable comments that have helped to improve the quality of the paper. P.B. should like to thank Prof. Paul Carling and Dr. Joris Heyman for their friendship and fruitful discussions on sediment transport.

## Appendix A. Approximate Riemann solver

The Jacobian matrix of (30) reads

$$\mathbf{J} = \frac{\partial \mathbf{F}}{\partial \mathbf{U}} = \begin{pmatrix} 0 & 1 & 0 & 0 \\ gh - \bar{v}^2 & 2\bar{v} & 0 & 0 \\ -\frac{\beta \bar{v} b}{h} & \frac{\beta b}{h} & \beta \bar{v} & 0 \\ 0 & 0 & 0 & 0 \end{pmatrix}. \quad (\text{A.1})$$

The eigenvalues  $s^p$  of (A.1) are given by the diagonal entries of  $\mathbf{\Lambda} = \mathbf{P}\mathbf{J}\mathbf{P}^{-1}$  and the corresponding right eigenvectors  $\mathbf{r}^p$  by the column vectors of  $\mathbf{P}$  with

$$\mathbf{\Lambda} = \begin{pmatrix} \bar{v} + c & 0 & 0 & 0 \\ 0 & \bar{v} - c & 0 & 0 \\ 0 & 0 & \beta \bar{v} & 0 \\ 0 & 0 & 0 & 0 \end{pmatrix}, \quad (\text{A.2})$$

$$\mathbf{P} = \begin{pmatrix} 1 & 1 & 0 & 0 \\ \bar{v} + c & \bar{v} - c & 0 & 0 \\ \frac{g\beta b}{c(c + \bar{v} - \beta \bar{v})} & \frac{g\beta b}{c(c - \bar{v} + \beta \bar{v})} & 1 & 0 \\ 0 & 0 & 0 & 1 \end{pmatrix}, \quad (\text{A.2})$$

in which  $c = \sqrt{gh}$ . The states  $\mathbf{u}$  in the Riemann problem correspond to the reconstructed interface values of  $\mathbf{U}_i$  from the fifth order component-wise weighted essentially non-oscillatory (WENO) scheme [53]. In Section 4.2 we will discuss the performance of the WENO scheme including an approximate Riemann solver for the discretization of the convective operator in the stochastic PDE of the Poisson density  $b$ . The discussion will be based on a thorough comparison between the numerical simulations and theoretical solutions derived by Ancey et al. [3]. The spatial jumps  $\Delta \mathbf{u} = \mathbf{u}_r - \mathbf{u}_l$  of reconstructed conservative variables with right and left states  $\mathbf{u}_r$  and  $\mathbf{u}_l$  were decomposed in terms of the eigenvectors  $\mathbf{r}^p$  or waves  $\mathcal{W}^p$  as

$$\Delta \mathbf{u} = \mathbf{u}_r - \mathbf{u}_l = \sum_p \alpha_p \mathbf{r}^p = \sum_p \mathcal{W}^p \quad (\text{A.3})$$

with

$$\alpha_1 = \frac{(c - \bar{v}) \Delta h + \Delta h \bar{v}}{2c}, \quad \alpha_2 = \frac{(c + \bar{v}) \Delta h - \Delta h \bar{v}}{2c},$$

$$\alpha_3 = \Delta b + \frac{1}{2c} (P_{31} - P_{32})(\bar{v} \Delta h - \Delta h \bar{v}) - \frac{1}{2} (P_{31} + P_{32}) \Delta h,$$

$$\alpha_4 = \Delta y_b. \quad (\text{A.4})$$

The fluctuations are computed using a Roe solver with entropy fix as described in [57]. Following the same procedure as for the shallow water equations, we derive the Roe averages for (30)

$$\tilde{h} = \frac{1}{2} (h^L + h^R), \quad \tilde{c} = \sqrt{g\tilde{h}}, \quad \tilde{v} = \frac{\bar{v}^L \sqrt{h^L} + \bar{v}^R \sqrt{h^R}}{\sqrt{h^L} + \sqrt{h^R}},$$

$$\frac{\tilde{b}}{\tilde{h}} = \frac{b^L \sqrt{h^R} + b^R \sqrt{h^L}}{h^L \sqrt{h^R} + h^R \sqrt{h^L}}. \quad (\text{A.5})$$

The left and right states of the flow depth  $h^{L,R}$  were corrected using the hydrostatic reconstruction by Audusse et al. [6] as described in Xing and Shu [79],

$$h^L \leftarrow \max(0, h^L + y_b^L - \max(y_b^L, y_b^R)),$$

$$h^R \leftarrow \max(0, h^R + y_b^R - \max(y_b^R, y_b^L)). \quad (\text{A.6})$$

The flux correction in the hydrostatic reconstruction was shifted to the source term in our implementation. The values (A.5)–(A.6) were used when evaluating (A.1)–(A.4).

It is worth commenting that the eigenvalues  $\Lambda$  and eigenvectors  $\mathbf{P}$  matrices (A.2) and consequently the waves  $\mathcal{W}$  in (36) do not coincide with those obtained in former deterministic Saint-Venant-Exner equations in which the Jacobian matrix depends at leading order on the adopted bed load formula, see e.g. Murillo and García-Navarro [63] and Juez et al. [45]. Furthermore, the dynamics of the sediment particles is influenced in our model not only by the advection velocity (or the waves  $\mathcal{W}$  of the hyperbolic subproblem) but also by the diffusive sediment transport mechanism, the erosion and deposition rates and the stochastic Wiener process which are basic in the developments of anti-dunes, as shown in Sections 3 and 4.

## Appendix B. Stochastic-deterministic source terms

Taking into account the numerical considerations on the source terms established in Section 4.1, the cell averaged source terms read

$$\mathbf{S}_i \approx \frac{1}{\Delta x} \int_{C_i} \mathbf{S}(x, t) dx \approx \begin{pmatrix} 0 \\ g \tilde{y}_b \tilde{\Delta} y_s + g \tilde{\Delta} \left( \frac{y_b^2}{2} - y_s y_b \right) - \frac{\tilde{\tau}_b}{\rho} \\ \lambda'_i - \kappa b_i + \sqrt{2 \mu} b_i \xi_b(x_i, t_n) \\ (\kappa V_p B^{-1} \langle b \rangle_i - \lambda_i) / (1 - \zeta_b) \end{pmatrix} \quad (\text{B.1})$$

in which

$$\tilde{y}_b = \frac{y_{b,i+\frac{1}{2}}^* + y_{b,i-\frac{1}{2}}^*}{2}, \quad \tilde{\Delta} y_s = \frac{y_{s,i+\frac{1}{2}}^L - y_{s,i-\frac{1}{2}}^R}{\Delta x},$$

$$\tilde{\Delta} \left( \frac{y_b^2}{2} - y_s y_b \right) = \frac{\left( y_{b,i+\frac{1}{2}}^* \right)^2 - \left( y_{b,i-\frac{1}{2}}^* \right)^2}{2 \Delta x} - \frac{y_{s,i+\frac{1}{2}}^L y_{b,i+\frac{1}{2}}^* - y_{s,i-\frac{1}{2}}^R y_{b,i-\frac{1}{2}}^*}{\Delta x},$$

$$\frac{\tilde{\tau}_b}{\rho} = \frac{\tau_{b,i}/\rho}{1 - \frac{\Delta t}{\rho} \frac{\partial \tau_{b,i}}{\partial h \bar{v}}} = \frac{f_i h_i \bar{v}_i |\bar{v}_i|}{2 (4 h_i + \Delta t f_i |\bar{v}_i|)}. \quad (\text{B.2})$$

In the deterministic shallow water equations the bed elevation was evaluated as  $y_{b,i+1/2}^* = \max(y_{b,i+1/2}^L, y_{b,i+1/2}^R)$  to ensure the well-balanced property in equivalent manner with Xing and Shu [79]. In contrast, in the stochastic partial differential equations of the  $b$ -variable we used an explicit pointwise evaluation of the source terms as usually done in the Euler–Maruyama scheme [55].

The individual entrainment rate  $\lambda'_i$  is evaluated in (B.1) from the volumetric flux of individual entrained particles per unit of bed area  $\lambda$  given, for instance, by Eq. (17):

$$\lambda'_i = \frac{B}{V_p} \lambda(\tau_{b,i}). \quad (\text{B.3})$$

The differential rate  $\kappa$  between deposition and collective entrainment rates is set to the constant value (16). For the sake of simplicity, the collective entrainment rate  $\mu$  is set to a constant value in the examples presented in Section 4. The noise term is computed as  $\xi_b(x_i, t_n) = \text{rnd} / \sqrt{\Delta t \Delta x}$  where  $\text{rnd}$  denotes a  $m$ -dimensional standard normally distributed random variable with zero mean value and unity standard deviation [41]. It was generated with `vdRngGaussian` Intel® subroutine. The last step in the source terms' discretization is the evaluation of  $\langle b \rangle_i$  and  $\lambda_i$ , which was achieved by taking the time averaging the cell values.

## References

- [1] Ancey C. Stochastic modeling in sediment dynamics: Exner equation for planar bed incipient bed load transport conditions. *J Geophys Res* 2010;115:F00A11.

- [2] Ancey C, Böhm T, Jodeau M, Frey P. Statistical description of sediment transport experiments. *Phys Rev E* 2006;74:011302.
- [3] Ancey C, Bohorquez P, Heyman J. Stochastic interpretation of the advection diffusion equation and its relevance to bed load transport. *J Geophys Res* 2015; submitted for publication.
- [4] Ancey C, Davison AC, Böhm T, Jodeau M, Frey P. Entrainment and motion of coarse particles in a shallow water stream down a steep slope. *J Fluid Mech* 2008;595:83–114.
- [5] Ancey C, Heyman J. A microstructural approach to bed load transport: mean behaviour and fluctuations of particle transport rates. *J Fluid Mech* 2014;744:129–68.
- [6] Audusse E, Bouchut F, Bristeau M-O, Klein R, Perthame B. A fast and stable well-balanced scheme with hydrostatic reconstruction for shallow water flows. *SIAM J Sci Comput* 2004;25:2050–65.
- [7] Audusse E, Boyaval S, Gao Y, Hilhorst D. Numerical simulations of the periodic inviscid Burgers with stochastic forcing. *ESAIM Proc Surv* 2015;48:308–20.
- [8] Bagnold R. An approach to the sediment transport problem from general physics. Professional paper 422-I, United States Geological Survey 1966.
- [9] Bagnold RA. The nature of saltation and of 'bed load' transport in water. *Proc R Soc London ser A* 1973;332:473–504.
- [10] Balmforth NJ, Provenzale A. Patterns of dirt. In: Balmforth NJ, Provenzale A, editors. *Geomorphological fluid mechanics*. Berlin: Springer Verlag; 2001. p. 369–93.
- [11] Balmforth NJ, Vakil A. Cyclic steps and roll waves in shallow water flow over an erodible bed. *J Fluid Mech* 2012;695:35–62.
- [12] Bernd AB, Harris RC. From data to probability densities without histograms. *Comput Phys Commun* 2008;179:443–8.
- [13] Bohorquez P. Competition between kinematic and dynamic waves in floods on steep slopes. *J Fluid Mech* 2010;645:375–409.
- [14] Bohorquez P, Fernandez-Feria R. Transport of suspended sediment under the dam-break flow on an inclined plane bed of arbitrary slope. *Hydrolog Process* 2008;22:2615–33.
- [15] Bohorquez P, Rentschler M. Hydrodynamic instabilities in well-balanced finite volume schemes for frictional shallow water equations. The kinematic wave case. *J Sci Comput* 2011;48:3–15.
- [16] Caleffi V, Aliani A, Bernini A. High-order balanced CWENO scheme for movable bed shallow water equations. *Adv Water Resour* 2007;30(4):730–41.
- [17] Camporeale C, Ridolfi L. Modal versus nonmodal linear stability analysis of river dunes. *Phys Fluids* 2011;23:104102.
- [18] Cao Z, Hu P, Hu K, Pender G, Liu Q. Modelling roll waves with shallow water equations and turbulent closure. *J Hydraul Res* 2015;53(2):161–77.
- [19] Carling PA, Shvidchenko AB. A consideration of the dune: antidune transition in fine gravel. *Sedimentology* 2002;49:1269–82.
- [20] Cartigny MJB, Ventra D, Postma G, van Den Berg JH. Morphodynamics and sedimentary structures of bedforms under supercritical-flow conditions: new insights from flume experiments. *Sedimentology* 2014;61(3):712–48.
- [21] Charru F. Selection of the ripple length on a granular bed sheared by a liquid flow. *Phys Fluids* 2006;18:121508.
- [22] Charru F. *Hydrodynamic instabilities*. Cambridge: Cambridge University Press; 2011.
- [23] Chatanantavet P, Whipple KX, Adams MA, Lamb MP. Experimental study on coarse grain saltation dynamics in bedrock channels. *J Geophys Res F* 2013;118:1161–76.
- [24] Cho H, Venturi D, Karniadakis GE. Statistical analysis and simulation of random shocks in stochastic Burgers equation. *Proc R Soc A* 2014;470:20140080.
- [25] Colebrook CF. Turbulent flow in pipes with particular reference to the transition region between the smooth- and rough-pipe laws. *J Inst Civ Eng* 1939;11:133–56.
- [26] Colombini M. Revisiting the linear theory of sand dune formation. *J Fluid Mech* 2004;502:1–16.
- [27] Colombini M. A decade's investigation of the stability of erodible stream beds. *J Fluid Mech* 2014;756:1–4.
- [28] Colombini M, Stocchino A. Ripple and dune formation in rivers. *J Fluid Mech* 2011;673:121–31.
- [29] Cordier S, Le MH, Morales de Luna T. Bedload transport in shallow water models: why splitting (may) fail, how hyperbolicity (can) help. *Adv Water Resour* 2011;34:980–9.
- [30] Cui Y, Parker G, Lisle TE, Pizzuto JE, Dodd AM. More on the evolution of bed material waves in alluvial rivers. *Earth Surf Process Landforms* 2005;30:107–14.
- [31] Dressler R. New nonlinear shallow-flow equations with curvature. *J Hydraul Res* 1978;16:205–22.
- [32] Durán O, Andreotti B, Claudin P. Numerical simulation of turbulent sediment transport, from bed load to saltation. *Phys Fluids* 2012;24:103306.
- [33] Einstein H. The bed-load function for sediment transportation in open channel flows. Technical Report No 1950/1026. United States Department of Agriculture.
- [34] Fernandez Luque R, van Beek R. Erosion and transport of bed-load sediment. *J Hydraul Res* 1976;14:127–44.
- [35] Fourrière A, Claudin P, Andreotti B. Bedforms in a turbulent stream: formation of ripples by primary linear instability and of dunes by nonlinear pattern coarsening. *J Fluid Mech* 2010;649:287–328.
- [36] Furbish DJ, Haff PK, Roseberry JC, Schmeckle MW. A probabilistic description of the bed load sediment flux: 1. Theory *J Geophys Res* 2012;117:F03031.
- [37] García MH. Sediment transport and morphodynamics. In: García MH, editor. *Sedimentation Engineering*. Vol. ASCE Manuals and Reports on Engineering Practice 110. Reston: American Society of Civil Engineers; 2007. p. 21–164.
- [38] Gardiner CW. *Handbook of stochastic methods*. Berlin: Springer Verlag; 1983.

- [39] Gilbert GK. The transportation of debris by running water. *US Geol Surv Prof Pap* 1914;86:263.
- [40] Glaister P. Approximate Riemann solutions of the shallow water equations. *J Hydraul Res* 1988;26:293–306.
- [41] Hairer M, Voss J. Approximations to the stochastic Burgers equation. *J Nonlinear Sci* 2011;21:897–920.
- [42] Hassan MA, Smith BJ, Hogan DL, Luzi DS, Zimmermann AE, Eaton BC. Sediment storage and transport in coarse bed streams: scale considerations. In: Habersack H, Piegay H, Rinaldi M, editors. *Gravel-bed rivers VI: from process understanding to river restoration*. Elsevier B.V.; 2008. p. 473–96.
- [43] Heyman J, Ma HB, Mettra F, Ancey C. Spatial correlations in bed load transport: evidence, importance, and modeling. *J Geophys Res* 2014;119:1751–67.
- [44] Huerre P, Monkewitz PA. Local and global instabilities in spatially developing flows. *Annu Rev Fluid Mech* 1990;22:473–537.
- [45] Juez C, Murillo J, García-Navarro P. A 2D weakly-coupled and efficient numerical model for transient shallow flow and movable bed. *Adv Water Resour* 2014;71:93–109.
- [46] Julien P-Y. *Erosion and Sedimentation*, 2nd ed. Cambridge: Cambridge University Press; 2010.
- [47] Juniper MP. The effect of confinement on the stability of two-dimensional shear flows. *J Fluid Mech* 2006;565:171–95.
- [48] Juniper MP, Hanifi A, Theofilis V. Modal stability theory. *Appl Mech Rev* 2014;66:024804.
- [49] Kalinske A. Movement of sediment as bed-load in rivers. *Trans Am Geophys Union* 1947;28:615–20.
- [50] Karniadakis G.E., Kirby II R.M. *Parallel scientific computing in C++ and MPI*. Cambridge University Press. 2003.
- [51] Kennedy J. The formation of sediment ripples, dunes, and antidunes. *Annu Rev Fluid Mech* 1969;1:147–68.
- [52] Ketcheson DI, LeVeque RJ. WENOCLAW: a higher order wave propagation method. In: Benzoni-Gavage S, Serre D, editors. *Hyperbolic problems: theory, numerics, applications*. Springer; 2008. p. 609–16.
- [53] Ketcheson DI, Parsani M, LeVeque RJ. Higher order wave propagation algorithms for hyperbolic systems. *SIAM J Sci Comput* 2013;35(1):A351–77.
- [54] Kleinhans M, van Rijn L. Stochastic prediction of sediment transport in sand-gravel bed rivers. *J Hydraul Eng* 2002;128:412–25.
- [55] Kloeden PE, Platen E. *Numerical solution of stochastic differential equations*. 3rd ed. Springer; 1999.
- [56] Lajeunesse E, Malverti L, Charru F. Bed load transport in turbulent flow at the grain scale: experiments and modeling. *J Geophys Res* 2010;115:F04001.
- [57] LeVeque RJ. *Finite volume methods for hyperbolic problems*. Cambridge: Cambridge University Press; 2002.
- [58] LeVeque RJ. A well-balanced path-integral  $f$ -wave method for hyperbolic problems with source terms. *J Sci Comput* 2011;48:209–26.
- [59] Liang Q, Marche F. Numerical resolution of well-balanced shallow water equations with complex source terms. *Adv Water Resour* 2009;32:873–84.
- [60] Lyn DA, Altinakar M. St. Venant–Exner equations for near-critical and transcritical flows. *J Hydraul Eng* 2002;128(6):579–87.
- [61] Majda A, Osher S. Propagation of error into regions of smoothness for accurate difference approximations to hyperbolic equations. *Comm Pure Appl Math* 1977;30:671–705.
- [62] Mettra F. *Morphodynamic mechanisms in steep channels: from local processes to large-scale evolution*; 2014. LHE/EPFL, <http://dx.doi.org/10.5075/epfl-thesis-6065>.
- [63] Murillo J, García-Navarro P. An Exner-based coupled model for two-dimensional transient flow over erodible bed. *J Comput Phys* 2010;229(23):8704–32.
- [64] Needham D, Merkin J. On roll waves down an open inclined channel. *Proc R Soc London* 1984;394:259–78.
- [65] Parker G, Seminara G, Solari L. Bed load at low Shield stress on arbitrarily sloping beds: alternative entrainment formulation. *Water Resour Res* 2003;39:1183.
- [66] Postacchini M, Brocchini M, Mancinelli A, Landon M. A multi-purpose, intra-wave, shallow water hydro-morphodynamic solver. *Adv Water Resour* 2012;38:13–26.
- [67] Recking A, Bacchi V, Naaim M, Frey P. Antidunes on steep slopes. *J Geophys Res* 2009;114:F04025.
- [68] Recking A, Liébault F, Peteuil C, Jolimet T. Testing bedload transport equations with consideration of time scales. *Earth Surf Process Landforms* 2012;37:774–89.
- [69] Ridolfi L, D’Odorico P, Laio F. Noise-induced phenomena in the environmental sciences. Cambridge University Press; 2011.
- [70] Roulund A, Sumer BM, Fredsøe J, Michelsen J. Numerical and experimental investigation of flow and scour around a circular pile. *J Fluid Mech* 2005;534:351–401.
- [71] Schmid PJ, Henningson DS. *Stability and transition in shear flows*. Springer; 2001.
- [72] Siviglia A, Stecca G, Vanzo D, Zolezzi G, Toro EF, Tubino M. Numerical modelling of two-dimensional morphodynamics with applications to river bars and bifurcations. *Adv Water Resour* 2013;52:243–60.
- [73] Sun H, Chen D, Zhang Y, Chen L. Understanding partial bed-load transport: experiments and stochastic model analysis. *J Hydrol* 2015;521:196–204.
- [74] Valiani A, Begnudelli L. Divergence form for bed slope source term in shallow water equations. *J Hydraul Eng* 2006;132(7):652–65.
- [75] Van Rijn LC. *Principles of sediment transport in rivers, estuaries and coastal seas*, 1006. Aqua publications Amsterdam; 1993.
- [76] Vesipa R, Camporeale C, Ridolfi L. A shallow-water theory of river bedforms in supercritical conditions. *Phys Fluids* 2012;24:094104.
- [77] Vesipa R, Camporeale C, Ridolfi L, Chomaz JM. On the convective-absolute nature of river bedform instabilities. *Phys Fluids* 2014;26:124104.
- [78] Wu W. *Computational river dynamics*. London: Taylor & Francis; 2007.
- [79] Xing Y, Shu C-W. High-order finite volume WENO schemes for the shallow water equations with dry states. *Adv Water Resour* 2011;34:1026–38.
- [80] Yalin MS, da Silva AMF. *Fluvial processes*. The Netherlands: IAHR Monograph, IAHR, Delft; 2001.